Neutron Laue Diffraction of Multi-Ferroic $MnWO_4$ in High Magnetic Fields.

We have succeeded in the time-of-flight neutron Laue diffraction in pulsed high magnetic fields at the Spallation Neutron Source. The phase diagram of the multiferroic material MnWO4 has been determined up to 30 T. The control of the field-pulse timing enabled an exploration of magnetic Bragg scattering through the time dependent of the neutron wavelength. This allowed us to observe several magnetic Bragg peaks with a single instrument configuration.

Neutron diffraction is an essential probe of magnetic structures and phase diagrams of magnetic materials. When a magnetic material has competing interactions, it may result in macroscopically degenerate ground state. For such cases, application of a magnetic field may lift the degeneracy and the interplay between spin, charge, orbital, and lattice degrees of freedom lead to rich phase diagram in magnetic field. A system of current interest is multiferroic, in which ferroelectric and a non-collinear magnetic structure are in tight relationship. The determination of a magnetic field phase diagram of such system is crucial to its understanding, and the neutron diffraction in high magnetic fields is expected to yield important insights.

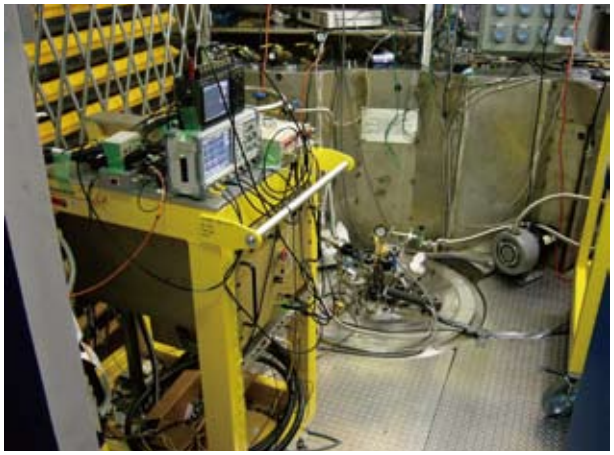

Fig. 1 The picture of the experimental system installed in SEQUOIA spectrometer at SNS. In the left-hand side, a compact capacitor bank is in the rack. The top of the cryostat insert is in the center.

Conventional neutron diffraction studies are possible in a steady magnetic field of 17 T, at the Helmholtz Zentrum Berlin[1]. Recently, a monochromatic neutron diffraction in a pulsed magnetic field up to 30 T was carried out using a reactor-based neutron source [2, 3]. In reactor experiment, a continuous beam of monochromatic neutrons was used and a single position in reciprocal space was investigated. An advantage of this method is its ability to continuously monitor the magnetic field dependence of intensity. Typically 100 to 200 field pulses are required at each point and the scanning in the reciprocal space to explore unknown Bragg spot is not practical in this method.

To overcome this difficulty, we have combined a pulsed magnetic field with a pulsed white neutron beam, employing wavelength-resolved diffraction based on neutron time-of-flight method. Here, we present the first application of neutron Laue diffraction in pulsed magnetic fields, using a white neutron beam at the Spallation Neutron Source: SNS of Oak Ridge National Laboratory as the collaboration between the magnetism division of IMR and SNS[4].

Fig. 1 shows the picture of the experimental setup. A compact capacitor bank is used as a power supply and the special magnet insert and the sample mount developed at IMR are used for the magnetic field generation. The system is so small and thus is portable as fitting to a check-in suitcase of air career. This feature enables us to conduct a visiting experiment in abroad easily.

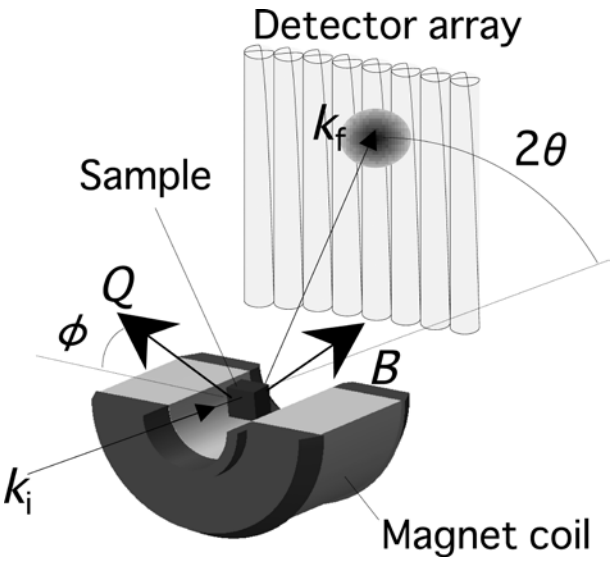

Fig. 2 The arrangement of the magnet and the detector. The scattering vector is nearly perpendicular to the magnetic field.

The cut view of the pulsed magnet and the arrangement of the detectors are shown in the Fig. 2. The magnetic field is nearly perpendicular to the scattering vector in the forward scattering configuration. When the detector is set in the backward position, the scattering vector is parallel to the magnetic field. The use of two different scattering geometries would be useful to investigate the directions of magnetic moments.

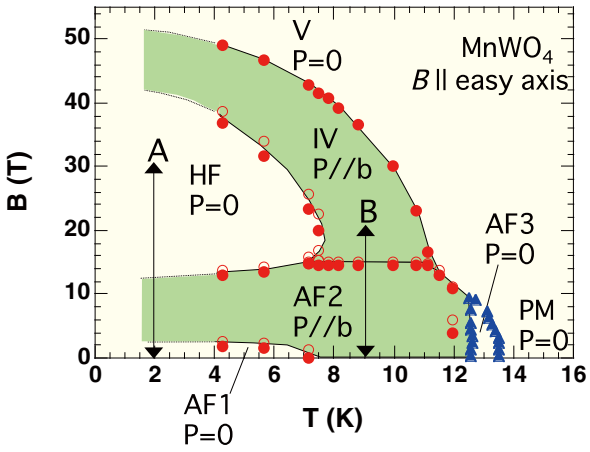

Fig. 3 The magnetic phase diagram of $MnWO_4$. The colored area is ferroelectric. The re-entrant phase transition takes place in the magnetic field scan at low temperature as shown by the arrow A.

As the first target of the investigation, we have selected a $MnWO_4$, which shows a complicated magnetic field-temperature phase diagram as shown in Fig. 3. There are at least 6 phases and some of them are expected to be incommensurate structure with ferroelectric states.

Fig. 4 shows the example of a time of flight spectrum, a pulsed magnetic field and Laue pattern of neutron diffraction. According to the conventional macroscopic magnetization measurement, the phase boundary between the AF2 Anti- ferromagentic phase colored by green and the HF phase is located at 12 T. The determination of the HF phase and the IV phase have not been made for the lack of high magnetic field neutron diffraction system.

In Fig. 4, the two peaks are found in the time of flight spectrum and the two Laue spots are corresponding to these peaks. As clearly indicated in this example, an advantage of Laue method is in its ability to map the reciprocal space. It is powerful to determine the magnetic field dependence of some incommensurate wave vector. In fact, by repeating a magnetic field scan at different temperatures and at different timings, we could determine the wave vector of the HF and the IV phases. It shows the powerfulness of the present experimental system.

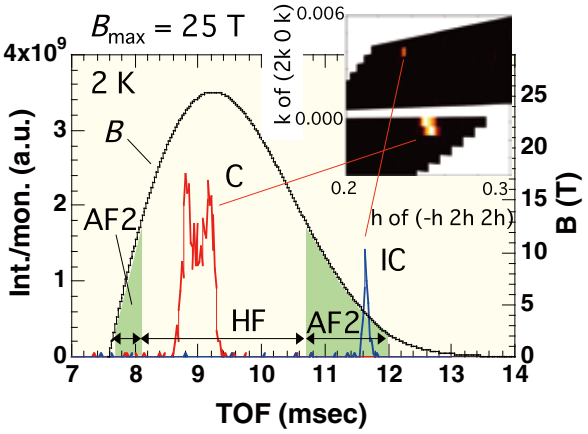

Fig. 4 The waveform of a pulsed magnetic field and the time of flight spectrum. The time integrated image of Laue pattern is in the right upper side. The two spots are C: commensurate and IC: incommensurate peaks as indicated by the lines. Two phases can be examined simultaneously by using the time dependent magnetic field.

To be summarized, we have succeeded in the high magnetic field neutron Laue diffraction for the first time. The usefulness of the method has been proven as the determination of complicated magnetic structure in multi-ferroic $MnWO_4$. It is notable that the highly positive remark is made for the present work [5].

This work has been performed as the collaboration with Kimura laboratory at Osaka University, the neutron science division of SNS and McMaster University.

References

[1] M. Meissner et al., Neuron News. **12** (2001) 12.
[2] S.Yoshii et al., Phys. Rev. Lett. **103** (2009) 077203.
[3] M. Matsuda et al., Rev. Lett. **104** (2010) 047201.
[4] H. Nojiri et al., Rev. Lett. **106** (2011) 237202.
[5]http://blogs.physicstoday.org/thedayside/2011/07/whats-wrong-with-the-spallation-neutron-source.html

Keywords: magnetic property
H. Nojiri and S. Yoshii (Magnetism Division)
E-mail:nojiri@imr.tohoku.ac.jp
URL:http://www.hfpm.imr.tohoku.ac.jp

Surface Atomic Structure and Vortex State in Iron-Based Superconductor $Ba(Fe_{0.93}Co_{0.07})_2As_2$

Scanning tunneling microscopy and spectroscopy (STM/STS) have been performed on the low-temperature cleaved surface of $Ba(Fe_{0.93}Co_{0.07})_2As_2$ single crystals. Two types of atomic surfaces are identified as the Ba-terminated 2×1 layer and As-terminated $\sqrt{2}\times\sqrt{2}$ layer. The superconducting gap, $2\Delta \simeq 6.9k_BT_c$, is observed only on the 2×1 layer surface; this value indicates the strong paring interaction. The glassy vortex structure without a long-range hexagonal order and the vortex core spectra without the zero bias conductance peak suggest a strong vortex pinning effect and a considerable degree of disorder.

The discovery of iron-pnictide superconductor [1] prompted extensive researches on a new class of high-T_c superconductors (HTSCs). In order to understand the complex physics in iron-based HTSCs, the direct observation of the superconducting electronic state is important. Scanning tunneling microscopy/spectroscopy (STM/STS) is a unique technique for detecting the electronic properties at the atomic scale, because STM is used to observe the atomic surface with sub-nanometer spatial resolution and STS provides information on the quasiparticle local density of states (LDOS). Thus, STM/STS is expected to play a crucial role in clarifying the electronic structure, mechanism of HTSC, and vortex–matter state in the magnetic field in iron-based HTSCs.

In this Research Highlight, we present STM/STS on iron-based superconductor $Ba(Fe_{0.93}Co_{0.07})_2As_2$ single crystals ($T_c \simeq 24$ K). The crystal structure of $Ba(Fe_{1-x}Co_x)_2As_2$ consists of an alternate stacking of Ba and FeAs layers. Since the chemical bonding between As and Fe ions is strong, the crystal is likely to cleave either between the Ba and As layers or within the Ba layer. Fig. 1(a) shows the STM topographic image of the $Ba(Fe_{0.93}Co_{0.07})_2As_2$ cleaved surface. The topographic image shows the step structure between two different atomic terraces. The bright and dark terraces correspond to the 2×1 surface (Fig. 1(b)) and the $\sqrt{2} \times \sqrt{2}$ surface (Fig. 1(c)), respectively. According to details of the atomic structure and a step height (~1.6 Å), it is concluded that the 2×1 surface is formed by half of the Ba atoms remaining on the As layer, and the $\sqrt{2} \times \sqrt{2}$ surface is the As layer from which Ba atoms are completely removed [2]. The superconducting (SC) tunneling spectra with the energy gap ($2\Delta \simeq 6.9k_BT_c$) are observed only on the 2×1 surface (see Fig. 1(d)); this value is approximately twice that for weak coupling s-wave BCS superconductors, indicating a strong pairing interaction similar to that observed in cuprate superconductors.

Fig. 2(a) shows the spectroscopic image in the magnetic field $H = 5$ T measured simultaneously with the STM topographic image in Fig. 1(a). This image maps the intensity of dI/dV at the energy of 7 meV, corresponding to the coherence peak. The upper left terrace is the non-SC $\sqrt{2} \times \sqrt{2}$ surface. Since the SC coherence peak is well developed at the bright region on the 2×1 surface, the dark spots indicated by circles can be identified as vortex

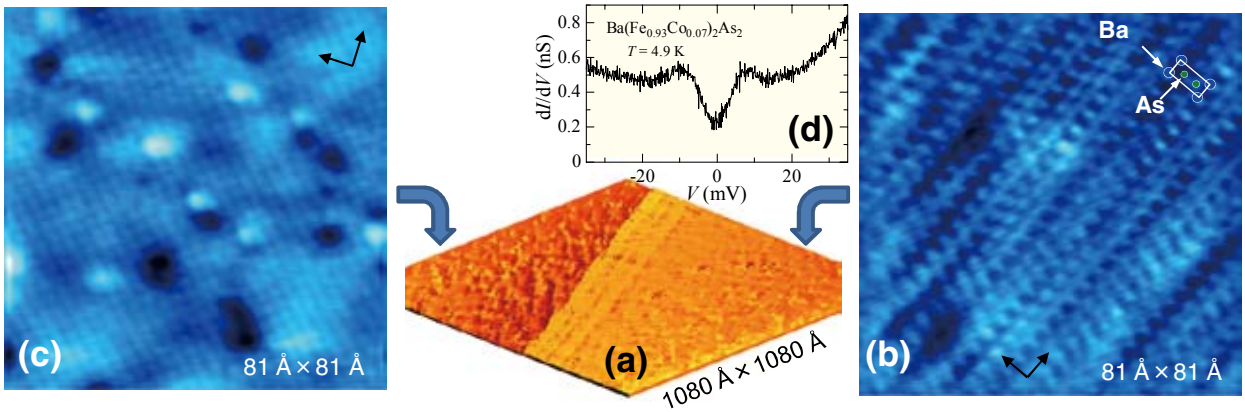

Fig. 1: (a) Constant-current STM image of cleaved surface of $Ba(Fe_{0.93}Co_{0.07})_2As_2$ single crystal ($V = 6.4$ mV, $I = 15$ pA). The fresh surface was prepared by the cleaving method at low temperatures below 20 K in the ultrahigh vacuum (UHV, ~10^{-10} Torr). The STM image shows the step structure between two different atomic surfaces. (b) Ba-terminated 2×1 surface. (c) As-terminated $\sqrt{2} \times \sqrt{2}$ surface. (d) Tunneling spectrum taken at the 2×1 surface.

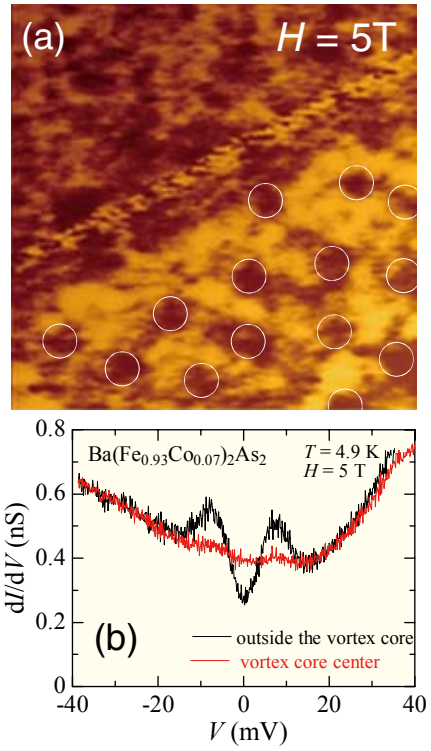

Fig. 2: (a) d*I*/d*V* image at 7 meV in the magnetic field 5 T obtained simultaneously with the STM image in 1(a). (b) d*I*/d*V* spectra at the center of and outside the vortex core.

cores. The average distance between the vortex cores (a_0 ~ 200-300 Å) is in good agreement with the calculated value (a_Δ = 215 Å) for the triangle vortex lattice at 5 T. The vortex core radius r_{av} ≃ 35-45 Å estimated is consistent with the Ginzburg-Landau coherence length $\xi(0)_{GL}$ ≃ 34 Å obtained from the upper critical field $H_{c2}(0) = \varphi_0/2\pi\xi_{GL}^2$ ≃ 28 T [3]. The vortex lattice shows the disordered structure with a short-range hexagonal order, but no translational or orientational order, indicating the vortex glass phase. Since there in no correlation between the vortex position and the surface morphology such as the 2×1 structure and surface defects, the vortex pinning center is not determined by STM/STS, suggesting bulk pinning deep inside the crystal and three-dimensionality of the vortex system. The disordered vortex structure due to strong pinning is supported by the large critical current density J_c ~ 2×10^5 A/cm^2 [3] and is consistent with previous STM/STS on $Ba(Fe_{0.9}Co_{0.1})_2As_2$ [4] and small angle neutron scattering (SANS) experiments on $Ba(Fe_{0.93}Co_{0.07})_2As_2$ [5].

As shown in Fig. 2(b), the d*I*/d*V* spectrum outside the vortex core shows SC characteristics, similar to the zero-field spectrum (see Fig. 1(d)). At the vortex core center, however, the coherence peak is reduced and the spectrum is nearly flat near the Fermi energy without the ZBC peak. The ZBC peak is a signature of the quasiparticle bound state for clean *s*-wave superconductors and gradually disappears with increasing disorder scattering. Thus, the vortex core spectroscopy indicates that $Ba(Fe_{0.93}Co_{0.07})_2As_2$ is not in the clean limit ($\xi_0 \ll \ell$); this result is supported by the comparability of the parameters between the mean free path $\ell = \hbar(3\pi^2)^{1/3}/e^2n^{2/3}\rho_0$ ~42 Å and the BCS coherence length ξ_0 ≃ 38-46 Å (i.e., ξ_0 ~ ℓ). Here, residual resistivity ρ_0 = 90 μΩcm [3], Hall coefficient R_H = 1 × 10^{-9} m^3/C [3], $\xi_{GL}(0) = 0.74\xi_0[\chi(0.88\xi_0/\ell)]^{1/2}$, and the Gor'kov function χ are used. The absence of the ZBC peak in $Ba(Fe_{0.93}Co_{0.07})_2As_2$ is consistent with previous STM/STS on $Ba(Fe_{0.9}Co_{0.1})_2As_2$, except for the V-shaped vortex-core spectrum [4], but is in sharp contrast to the recent experiment on hole-doped $(Ba_{0.6}K_{0.4})Fe_2As_2$ [6], which exhibits an ordered vortex-lattice and a quasiparticle bound state at a small negative-bias. These discrepancies can be explained by the difference in the degree of the disorder strength between in-plane doped $Ba(Fe_{0.93}Co_{0.07})_2As_2$ and out-of-plane doped $(Ba_{0.6}K_{0.4})Fe_2As_2$. The in-plane Co-doping on the Fe site enhances the disorder potential drastically in the superconducting FeAs layers. Since all vortices meet Co atoms (average distance: ~ 11 Å), the vortex structure and vortex-core electronic state are strongly modified by the disorder, in contrast to $(Ba_{0.6}K_{0.4})Fe_2As_2$ [6].

References

[1] Y. Kamihara, T. Watanabe, M. Hirano and H. Hosono, J. Am. Chem. Soc. 130, 3296 (2008).
[2] T. Nishizaki, Y. Nakajima, T. Tamegai, N. Kobayashi, J. Phys. Soc. Jpn. 80, 014710 (2011).
[3] Y. Nakajima, T. Taen and T. Tamegai, J. Phys. Soc. Jpn. 78, 023702 (2009).
[4] Y. Yin, M. Zech, T. L. Williams, X.F. Wang, G. Wu, X.H. Chen, and J.E. Hoffman, Phys. Rev. Lett. 102, 097002 (2009).
[5] P. Das, T.O'Brien, MLaver, C. D. Dewhurst, N. Ni, S. L. Bud'ko, P.C. Canfield and M.R. Eskildsen, Supercond. Sci. Technol. 23, 054007 (2010).
[6] L. Shan, Y.-L. Wang, B. Shen, B. Zeng, Y. Huang, A.Li, D. Wang, H. Yang, C. Ren, Q.-H. Wang, S. Pan, and H.-H. Wen, Nature Phys. 7, 325 (2011).

Keywords: high-Tc iron-based pnictide superconductors, scanning tunneling microscopy
T. Nishizaki and N. Kobayashi (Low Temperature Physics Division)
E-mail: terukazu@imr.tohoku.ac.jp
URL: http://ltp.imr.tohoku.ac.jp/

Anderson Localization Enhanced by Electron Correlations near Mott Transition

Randomness in the correlated electron system like as the low dimensional organic conductors is essentially important in real materials. The x-ray irradiation to an organic superconductor makes the superconducting state to the Anderson-type localization insulating state due to introducing the molecular disorder, while the sister organic compound having the Mott insulating ground state changes to the similar localization insulating state by the irradiation. These observations indicate that the stronger electron correlation upon approaching to the Mott transition enhances Anderson-type electron localization.

Metal-insulator transitions are of considerable importance for strongly correlated electron systems. Among the various types of the Metal-insulator transitions, the Mott transition due to electron-electron interactions is one of the most attractive phenomena [1]. Another way of the electron localization originates from the interference of the electron wave functions due to randomness. This is the Anderson insulator derived by introducing disorder into the material [2]. Since the randomness in the correlated electron system is essentially important in real materials, systematic studies of disorder effects are desired in systems nearby the Mott transition for understanding their physical properties.

Organic charge-transfer salts based on a donor molecule bis(ethylenedithio)-tetrathiafulvalene (abbreviated as BEDT-TTF) have been recognized as one of the highly correlated electron systems . Among them, κ-(BEDT-TTF)$_2$*A*, where *A* is anion molecule, has attracted considerable attention as a bandwidth-controlled Mott transition system. The crystal structure of κ-(BEDT-TTF)$_2$Cu[N(CN)$_2$]X (X = Br or Cl) is shown in Fig.1. Its remarkable feature is that the native quarter filled band is modified to the effective half filled band by the strong dimer structure consisting of two BEDT-TTF molecules. Thus this family of organic conductors has been considered as a typical bandwidth controlled Mott transition system with strongly correlated electrons [3]. One can control the strength of the electron correlation relative to the bandwidth by small pressure or partial molecule substitution, which leads to a Mott insulator-metal (superconductor) transition as shown latter in Fig. 3.

It has been known that x-ray irradiation to the organic materials causes molecular disorder and this remains permanently in organic molecules. Actually the molecular disorder in the organic superconductor κ-(BEDT-TTF)$_2$Cu(NCS)$_2$ causes an increase of the residual resistivity and then suppresses the superconductivity [4]. Recently, Sano et al. found that the weak molecular disorder introduced by x-ray irradiation to the organic superconductor κ-(BEDT-TTF)$_2$Cu[N(CN)$_2$]Br induced the Anderson-type localization insulating state from the strongly correlated metallic/superconducting state [5]. The latter salt having narrower bandwidth *W* is located nearby the Mott critical point in the metallic side in contrast to the former one with wider *W* (Fig. 3).

Fig. 2 shows the temperature dependence of the resistivity in the x-ray irradiated organic Mott insulator κ-(BEDT-TTF)$_2$Cu[N(CN)$_2$]Cl (upper

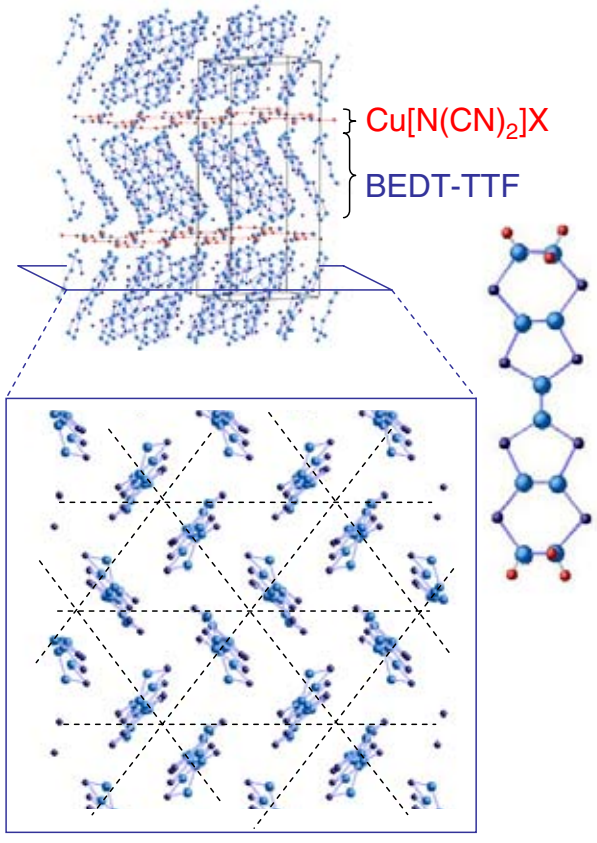

Fig. 1: Crystal structure of the organic superconductor κ-(BEDT-TTF)$_2$Cu[N(CN)$_2$]X. The BEDT-TTF conducting layers are sandwiched by the insulating anion Cu[N(CN)$_2$]X layers. In case of X = Br, it becomes the superconductor with T_c of 11 K, while the Mott insulating state appears with X = Cl. In the two dimensional BEDT-TTF layers, the molecules have a characteristic arrangement. The BEDT-TTF molecule dimers form the triangular lattice.

panel) and the organic superconductor κ-(BEDT-TTF)$_2$Cu[N(CN)$_2$]Br (lower panel). The samples are irradiated at 300 K using a non-filtered tungsten target at 40 kV and 20 mA, which corresponds to approximately 0.5 MGy/h. Introducing the molecular defect by the x-ray irradiation, the resistivity decreases and increases from the Mott insulating state and the superconducting state to the similar Anderson-type localization insulating state in κ-(BEDT-TTF)$_2$Cu[N(CN)$_2$]X with X = Cl and Br, respectively. In addition, the hydrostatic pressures to both the localization insulating states restore the metallic properties due to the broadening of the bandwidth. These observations indicate that the stronger electron correlation upon approaching to the Mott transition enhances Anderson-type electron localization due to disorder introduced by x-ray irradiation. Further studies like as the low energy spectroscopy on the competition and/or cooperation of the Mott and Anderson transitions close to the Mott critical point are important for understanding the critical behavior of the electrons in the real materials.

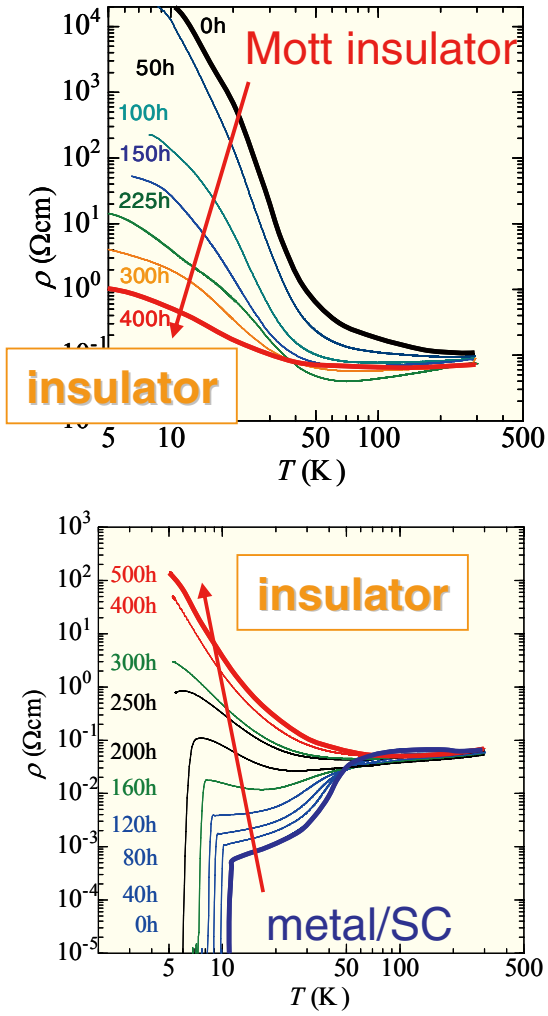

Fig. 2: Temperature dependence of the resistivity in the x-ray irradiated organic Mott insulator κ-(BEDT-TTF)$_2$Cu[N(CN)$_2$]Cl (upper panel) and the organic superconductor κ-(BEDT-TTF)$_2$Cu[N(CN)$_2$]Br (lower panel). The samples are irradiated at 300 K using a non-filtered tungsten target at 40 kV and 20 mA, which corresponds to approximately 0.5 MGy/h.

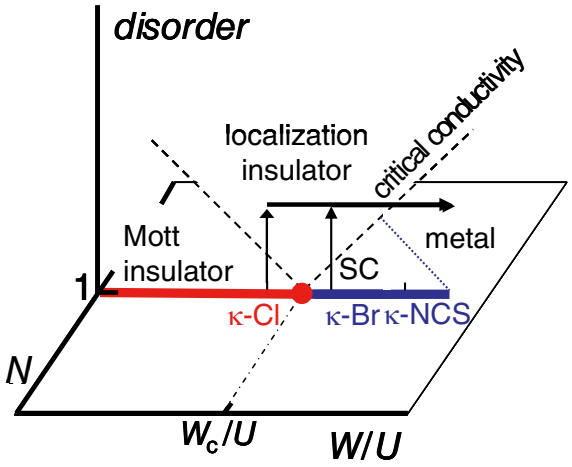

Fig. 3: Schematic phase diagram for band width *W*, carrier number *N* and disorder. The vertical and horizontal arrows represent the experimental processes of the x-ray irradiation for introducing disorder and then the application of pressure to increase *W*, respectively. Localization insulating state appears with weaker disorders by approaching Mott critical point.

References

[1] M. Imada, A. Fujimori and Y. Tokura, Rev. Mod. Phys. **70**, 1039 (1998) .
[2] P. W. Anderson, Phys. Rev. **109**, 1492 (1958).
[3] K. Kanoda, Hyperfine Interact. **104**, 235 (1997).
[4] J. G. Analytis, A. Ardavan, S. J. Blundell, R. L. Owen, E. F. Garman, C. Jeynes, and B. J. Powell, Phys. Rev. Lett. **96**, 177002 (2006).
[5] K. Sano, T. Sasaki, N. Yoneyama and N. Kobayashi, Phys. Rev. Lett. **104**, 217003 (2010).

Keywords: organic, superconducting, metal-insulator transition
T. Sasaki (Low temperature condensed state physics)
E-mail: takahiko@imr.tohoku.ac.jp
URL: http://cond-phys.imr.tohoku.ac.jp/

Doping Effects on the Stacking Fault Energy in Silicon

In silicon crystals, the width of a stacking fault ribbon bound by a pair of partial dislocations increases when n-type dopant atoms (phosphorus, arsenic, and antimony) segregate nearby the ribbon, while the width is unchanged when p-type dopant atoms (boron and gallium) segregate. The origin of the increase for n-type dopant atoms is the reduction of the stacking fault energy due to an electronic interaction between the ribbon and the dopant atoms segregating at the ribbon, rather than the reduction of the strain energy around the partial dislocations due to the dopant atoms segregating nearby the partials. The interaction energy is estimated to be 0.15±0.05 eV.

Grain boundaries and crystal interfaces including stacking faults are a key issue for high performance photovoltaic and/or electronic devices fabricated with silicon (Si) crystals, since they are frequently introduced in Si epilayers and miniaturized Si electronic devices, as well as polycrystalline Si such as cast Si for solar cells, during crystal growth and device fabrication. It is theoretically expected that a stacking fault interacts with point defects such as dopant atoms [1], and the interaction leads to a segregation of the defects (a so-called Suzuki segregation [2]). The interaction would modify the dopant distributions and electronic properties in Si with stacking faults. Also, dopant atoms segregating at a stacking fault ribbon bound by a pair of partial dislocations (a so-called dissociated dislocation) would assist the pinning of the dislocation motion [3, 4], as well as modify the energy levels of the stacking fault ribbon. In the present work, we have determined experimentally the segregation of various kinds of dopant atoms nearby stacking fault ribbons and evaluated the interaction energy [5-8].

Dislocation-free bulk single crystals of n-type Si doped with phosphorus (P) (with the concentration of 3×10^{19} cm^{-3}), arsenic (As) (1×10^{19} cm^{-3}), or antimony (Sb) atoms (5×10^{18} cm^{-3}), and those of p-type Si doped with boron (B) (2×10^{20} cm^{-3}) or gallium (Ga) (2×10^{18} cm^{-3}) atoms were grown by the Czochralski (CZ) method. The CZ crystals inevitably contained oxygen (O) atoms with a concentration about 10^{18} cm^{-3}. Also, P- (3×10^{19} cm^{-3}) or B- (8×10^{18} cm^{-3}) doped crystals without O impurities were grown by the floating zone (FZ) method. Dissociated dislocations lying on (111), in a density about 10^{9} cm^{-2}, were introduced in the crystals by plastic deformation at elevated temperature 1173 K for 0.5 h. The deformed crystals were then annealed at the same temperature for a period t_{an} up to 110 h without stress, so that dopant atoms could interact with dislocations via their thermal migration. The annealed crystals were characterized by weak-beam dark-field transmission electron microscopy (TEM).

In heavily-doped crystals annealed for a long period, radial strain fields about a few nm in diameter are observed nearby dissociated dislocations (Fig. 1). Since the strain fields increase in size with increasing t_{an} and they are not observed in lightly-doped crystals annealed for a short period, dopant atoms would segregate at dissociated dislocations during annealing, via their thermal migration, and lattice planes nearby the dislocations are distorted due to the agglomerates of the dopant atoms [5, 6]. The number density and the size of radial strain fields are similar in CZ- and FZ-crystals doped with P atoms in the same concentration, and this suggests that the segregation of O atoms is negligible in the present experimental condition [5].

The width of a stacking fault ribbon bound by a pair of partial dislocations is estimated with the intensity profile of the partials in TEM images taken into account the diffraction condition,

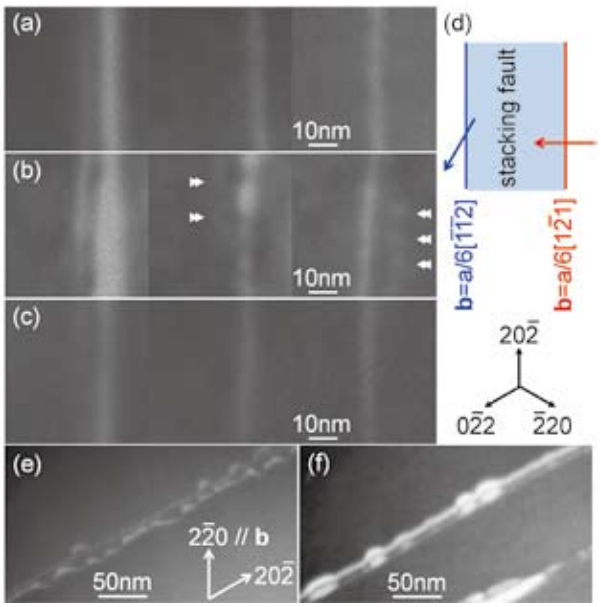

Fig. 1: A dissociated dislocation in CZ-Si crystals; doped with P (t_{an} = (a) 0.5 and (b) 10.5 h) or (c) non-doped (t_{an} = 10.5 h). The left, center, and right images in each figure are, respectively, taken with the reflection **g** = (0$\bar{2}$2), (2$\bar{2}$0), and (20$\bar{2}$). Double arrowheads in (b) indicate P agglomerates. The structural nature of each dislocation in (a–c) is schematically shown in (d). Segregation of (e) P (t_{an} = 110.5 h) and (f) Ga (t_{an} = 10.5 h) atoms nearby a dislocation.

and the apparent stacking fault energy γ is evaluated with the estimated width with an anisotropic elasticity theory [8]. The estimated γ are summarized as a function of the number of dopant atoms that can agglomerate nearby partials via their thermal migration N; N is defined as $N=\pi[(D_a t_{an})^{0.5}]^2 c_a$, in which D_a and c_a are, respectively, the diffusion constant and the concentration of a dopant atoms (Fig. 2). For n-type crystals, γ decreases with increasing N in the range up to about 5×10^2 nm^{-1}, and it is unchanged in the range above 5×10^2 nm^{-1}, irrespective of the growth method and the atomic number of dopant atoms [6, 7]. On the other hand, γ is unchanged with increasing N for p-type crystals [5].

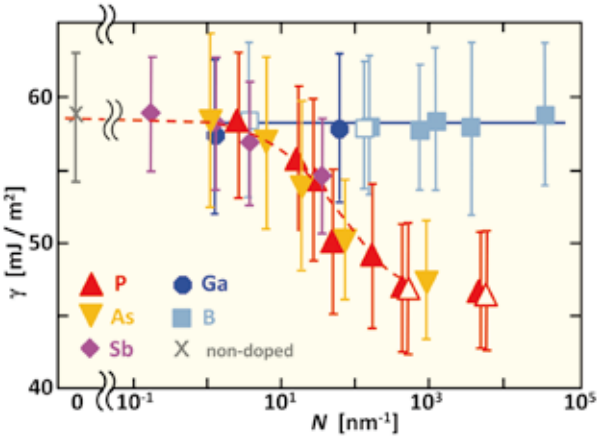

Fig. 2: The apparent stacking fault energy γ vs the number of dopant atoms that can agglomerate at dissociated dislocations N, for non-doped, p-type, and n-type crystals. Open and closed marks indicate the data for FZ- and CZ-crystals, respectively.

In heavily-doped crystals, the width of a stacking fault ribbon bound by a pair of partial dislocations would be different from the width in non-doped crystals, and it depends on the charge state and strain around the partials, as well as the stacking fault energy. The first effect, due to the ionization of partials via the Patel effect [9], is ignored in our heavily doped crystals since the Debye screening length is rather short (less than about 5 nm). Also, the second effect, due to the reduction of strain around partials via the segregation of dopant atoms, is negligible since the separation of a pair of partial dislocations is unchanged even when a number of Ga atoms segregate nearby the partials. The decrease of γ in n-type crystals is, therefore, due to an electronic interaction between a stacking fault ribbon and n-type dopant atoms resulting in the reduction of the stacking fault energy. Actually, ab-initio calculations indicate that P atoms would segregate at a stacking fault under an electronic interaction and the segregation results in the reduction of the stacking fault energy, while B atoms do not interact with stacking faults [5]. Also, 3D atom probe measurements reveal that [10], P and As atoms segregate but B atoms do not segregate at interfaces in poly-crystals.

As a simple model for the segregation of n-type dopant atoms at a stacking fault, γ could be written as $(1-p)\gamma_{Si}+p\gamma_{SiX}$, in which p indicates the occupation probability of X atoms (X: P, As, or Sb) at a stacking fault in thermal equilibrium, and γ_{Si} and γ_{SiX} are, respectively, the stacking fault energy in pure Si crystals and that in SiX crystals. The segregation probability p could be written as $p=1/[1+(1/C_0^*)\exp(-E/kT)]$, in which E is the interaction energy of an X atom with a stacking fault and C_0^* is the concentration of X atoms nearby the stacking fault, on the analogy of the segregation at a dislocation [4]. Considering that the probability p would reach the maximum at $N\sim5\times10^2$ nm^{-1} (Fig. 2), the interaction energy E is experimentally estimated to be 0.15±0.05 eV (the broken curve in Fig. 2) [5], and the estimated value is consistent with the theoretical result of 0.1 eV [1].

references

[1] J. F. Justo, A. Antonelli, T. M. Schmidt, & A. Fazzio, Physica B **273-274** (1999) 473.
[2] H. Suzuki, J. Phys. Soc. Jpn. **17** (1962) 322.
[3] I. Yonenaga, Mater. Sci. Eng. B **124–125** (2005) 293 .
[4] K. Sumino & I. Yonenaga, Solid State Phenom. **85/86** (2002) 145.
[5] Y. Ohno, Y. Tokumoto, H. Taneichi, K. Togase, S. R. Nishitani, & I. Yonenaga, Physica B (2011) in press.
[6] Y. Ohno, Y. Tokumoto, & I. Yonenaga, Thin Solid Films (2011) in press.
[7] Y. Ohno, T. Taishi, Y. Tokumoto, & I. Yonenaga, J. Appl. Phys. **108** (2010) 073514.
[8] Y. Ohno, T. Shirakawa, T. Taishi, & I. Yonenaga, Appl. Phys. Lett. **95** (2009) 091915.
[9] J. R. Patel, L. R. Testardi, & P. E. Freeland, Phys. Rev. B **13** (1976) 3548.
[10] K. Inoue, F. Yano, A. Nishida, H. Takamizawa, T. Tsunomura, Y. Nagai, & M. Hasegawa, Appl. Phys. Lett. **95** (2009) 043502.

Keywords: grain boundaries, dopant, transmission electron microscopy (TEM)
Yutaka Ohno (Physics of Crystal Defects)
E-mail: yutakaohno@imr.tohoku.ac.jp
URL:http://lab-defects.imr.tohoku.ac.jp

TOhoku Mixed Basis Orbitals *ab initio* Program (TOMBO)

Among many first-principles methods, all-electron mixed basis approach using both plane waves and numerical atomic orbitals confined inside non-overlapping atomic spheres has a distinct advantage to reduce the computational cost of all-electron electronic structure calculations of various kinds of systems, localized and extended systems, isolated and bulk systems, etc. with an enough high accuracy. This is our original method, which has been implemented in a program called TOMBO.

TOhoku Mixed Basis Orbitals *ab initio* program (TOMBO) is a tool for first principles calculations [1], which has been developed by Kawazoe Laboratory over 15 years. It is based on our original all-electron mixed basis approach [2-4], in which one electron wave functions are expressed by using both plane waves (PWs) and atomic orbitals (AOs). Since AOs are numerically defined inside the non-overlapping atomic spheres in radial (logarithmic) mesh, all-electron calculations with PWs can be performed very accurately with a modest computational cost. The number of PWs required in this method is significantly fewer than that required in standard pseudopotential or PAW methods. Moreover, one can avoid the problems such as the basis set superposition error (BSSE) appearing in standard LCAO methods and the overcompleteness problem appearing in standard mixed-basis methods. TOMBO can describe extended PW-like states as well as well localized core states with modest number of basis functions. It is applicable to various kinds of systems including atoms, molecules, clusters, surfaces, and crystals. Therefore, it has an apparent advantage compared to many preexisting first-principles methods. Using TOMBO, we can study, for example, with enough high accuracy, the properties affected by core levels such as the hyperfine structures [5].

To demonstrate an advantage of TOMBO, we show in Fig. 1 the dependence of (a) the C-H bond length (Å) and (b) the total energy (eV) of a CH_4 molecule on the cutoff energy (eV) of PWs used in the calculations. The curves correspond to the three different cases, where the following AOs are included in the calculations: 1s only (-○-), 1s and 2s (-□-), and 1s, 2s and 2p (-△-) for carbon. (For hydrogen, 1s AO is always included.) It is obvious from this figure that one can reduce the cutoff energy of PWs by introducing 1s, 2s, and 2p AOs for carbon; in this case (-△-), 300 eV of the cutoff energy is enough to obtain good convergence. This statement is general for any systems including hydrogen and carbon atoms, for which usually very high cutoff energy of PWs (typically, ~600 eV) is required in standard PW-based methods.

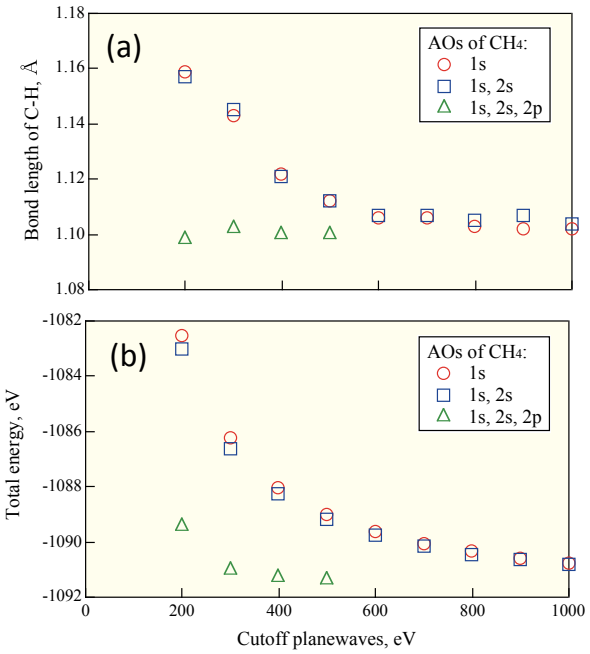

Fig.1 The dependence of (a) the bond length between C and H (Å) and (b) the total energy of an isolated CH_4 molecule on the cutoff energy of PWs (eV). Red circles, blue squares, and green triangles represent, respectively, the calculations with 1s AO only, 1s and 2s AOs, and 1s, 2s, and 2p AOs for the carbon atom.

Recently, we have applied TOMBO to the study of hydrogen storage materials [6]. To simulate useful structures, we introduced simple models of metal organic frameworks (MOFs) that can expand hydrogen storage capacity by lithium cation doping to clarify the physical mechanisms of enhancing hydrogen adsorption energy. Fig. 2 shows the optimized geometry of a useful calixarene structure (having a cup-like shape) including lithium atoms. We found that the adsorption of lithium atoms (red circles in the figures) increases the binding energy of incorporating hydrogen molecules much higher than the systems without lithium doping. Besides this study, by using high performance computers, we can simulate and design various kinds of new hydrogen storage materials composed by relatively light elements compared to the systems considered so far in the literatures.

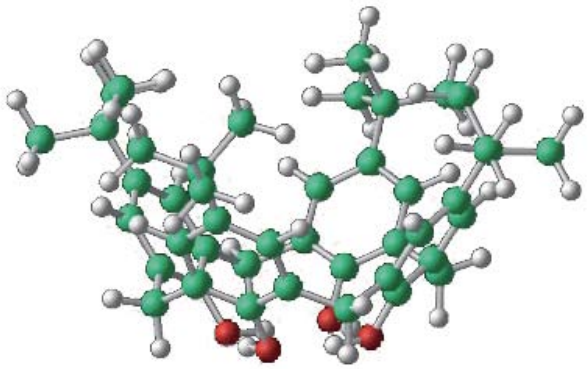

Fig.2 The optimized atomic geometry of a cup-like shaped calixarene doped with lithium ions.

Another interesting application of TOMBO is to simulate electron dynamics of an electronic excited state in materials. The time evolution of the electrons and holes in the electronic excited states can be treated by using TOMBO on the basis of the adiabatic local density approximation (adiabatic LDA) in the time-dependent density functional theory (TDDFT) combined with the Ehrenfest theorem for the adiabatic process. As a very simple example, we considered a possibility of dissociation of a hydrogen molecule around a nickel dimer. We put one hydrogen molecule and one nickel dimer in a skew position. When one electron is excited to the first excited state, where charge transfer occurs from hydrogen to nickel, we found that the hydrogen molecule starts to dissociate, and the distance between nickel and hydrogen atoms becomes shorter. In Fig. 3, dynamics of the dissociative process of a hydrogen molecule around a nickel dimer in the first (optically) excited state is traced in a red trajectory. The red point at the bottom (5.0Å, 4.0Å) denotes the nickel dimer pointing perpendicular to the figure plane. This dissociative trajectory of hydrogen atoms should be compared to the non-dissociative trajectory in the ground state (although not drown in the figure). This study supports to clarify the dynamics of the spill-over process in hydrogen storage materials, which may improve the hydrogen storage capacity to higher densities (6wt.% or more) in order to facilitate practical use [7].

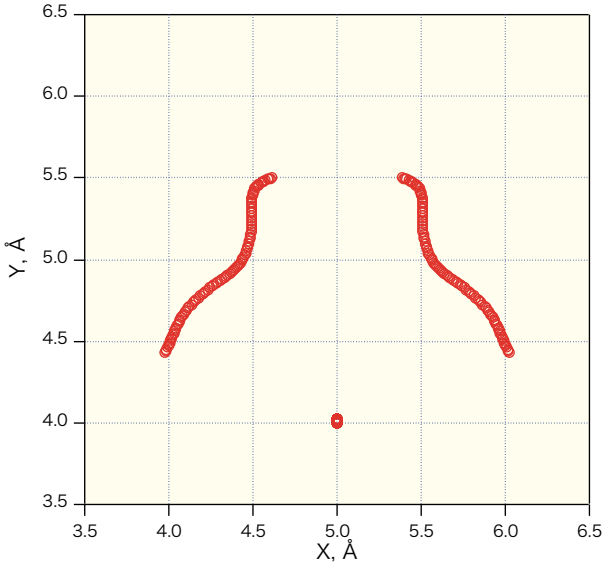

Fig.3 The trajectory (from up to down) of hydrogen atoms of a hydrogen molecule around a nickel dimer (pointing perpendicular to the figure plane) when one electron is excited from the highest occupied molecular orbital level to the lowest unoccupied molecular orbital level.

References

[1] A. Jain, V. Kumar, M. H. F. Sluiter, and Y. Kawazoe, Comp. Mat. Sci. **36**, 171 (2006).
[2] T. Ohtsuki, K. Ohno, K. Shiga, Y. Kawazoe, Y. Maruyama, and K. Masumoto, Phys. Rev. Lett. **81**, 967 (1998).
[3] K. Ohno, Y. Maruyama, H. Kamiyama, E. Bei, K. Shiga, Z.-Q. Li, K. Esfarjani, and Y. Kawazoe, in "Mesoscopic Dynamics of Fracture: Computational Materials Design", edited by H. Kitagawa, T. Aihara Jr., and Y. Kawazoe, Springer Series on Advances in Materials Research, Vol.1 (Springer-Verlag, Berlin, Heidelberg, 1998) pp.210-219.
[4] K. Ohno, K. Esfarjani, and Y. Kawazoe, "Computational Materials Science: From *Ab Initio* to Monte Carlo Methods", Springer Series in Solid-State Sciences, Vol.129 (Springer-Verlag, Berlin, Heidelberg, 1999) pp.1-325.
[5] M. S. Bahramy, M. H. F. Sluiter, and Y. Kawazoe, Phys. Rev. B **73**, 045111 (2006).
[6] R. Sahara, H. Mizuseki, and Y. Kawazoe, The Bulletin of the Society of NANO Science and Technology (in Japanese), **9** (2), 45 (2011).
[7] R. Sahara, K. Ohno, and Y. Kawazoe, in preparation.

Keywords: TOMBO, first-principles method, all-electron mixed basis approach
R. Sahara[1], M. H. F. Sluiter[2], K. Ohno[3], H. Mizuseki[1], and Y. Kawazoe[1]
1) IMR, Tohoku University, 2) Department of Materials Science and Engineering, Delft University of Technology, 3) Department of Physics, Yokohama National University
E-mail: kawazoe@imr.edu
URL: http://www.kawazoe.imr.edu

Nitride Semiconductors: Saving Our Planet

Nitride semiconductors such as InN, GaN, AlN and their alloys are very promising for fabricating devices with low power consumption, high-power, and high-frequency. InGaN-based blue light-emitting-diodes (LEDs) and laser-diodes (LDs) have been already commercially available. The new trends of nitride semiconductors in the region of deep ultraviolet, green, and infrared wavelength, will promote the device applications saving energy and creating new energies. Our researches are related with these new technology trends, challenging the nitride semiconductor-based LDs for the optical fiber communications system, phosphor-free white LEDs, brilliant green LEDs, and high-efficiency solar cells. One of the key tasks for implementing the above devices is to improve the crystalline quality of the InN film, using the pressurized-reactor metalorganic vapor phase epitaxy (PR-MOVPE) technology which has been developed by ourselves. This PR-MOVPE will become a strong tool for the thin film growth with high equilibrium pressure between gas and solid phases because the partial pressure of sources makes it possible to control the facets of growth islands. This effect is very important for getting high-quality epitaxial film grown on substrates with lattice mismatch between substrates and epitaxially grown films. In the case of nitride semiconductors, this pressure control is one of most important technology because blue, green, and ultraviolet LEDs are usually fabricated on sapphire substrates.

InN with a narrow band gap of about 0.65 eV can be expected as a novel material for LDs in optical communications systems because *dEg/dT* at room temperature can be expected to be smaller than that of InGaAsP [1] from the optical absorption measurement. Ideally, electron-phonon interactions mainly contribute to *dEg/dT*. *T*-dependent static correlation functions of vibrational atomic displacements $\langle u^2 \rangle$ of an InN film were measured by X-ray diffraction (XRD).

The measurements were carried out using a UHV chamber mounted on a six-circles diffractometer in SPring-8. A 200-nm-thick InN film, which was grown on (0001) sapphire substrates by PR-MOVPE [2], was cooled down to 60 K. Surface-normal and surface-parallel (radial and azimuthal) line scans in reciprocal space around 222 and 034 reflections of the InN film were repeatedly measured. *T*-dependent $\langle u^2 \rangle$ of wurtzite group-III nitrides have been calculated and fitted to the analytical form [3]

$$\left\langle u^2 \right\rangle = \frac{\hbar}{2m\omega} \coth\left[\frac{\hbar\omega}{2k_B T}\right], \quad (1)$$

where m is an atomic mass and ω is characteristic frequency expressed as

$$\omega = A\exp\left(-T^2/\sigma^2\right) + B. \quad (2)$$

The A, B and σ are parameters depending on element, displacement direction, and material [3]. X-ray diffraction intensity is proportional to square of the absolute value of the structure factor $F(\mathbf{q})$

$$F(\mathbf{q}) = f_{\mathrm{In}}(\mathbf{q})\exp\left(-M_{\mathrm{In}}(\mathbf{q})\right)\sum_j \exp\left(i\mathbf{q}\cdot\mathbf{r}_j^{\mathrm{In}}\right) + f_{\mathrm{N}}(\mathbf{q})\exp\left(-M_{\mathrm{N}}(\mathbf{q})\right)\sum_j \exp\left(i\mathbf{q}\cdot\mathbf{r}_j^{\mathrm{N}}\right), \quad (3)$$

where $\mathbf{q}$ is scattering vector, f_α is an atomic scattering factor, r_j^α is the position of j-th atom α (In or N), and M_α is expressed as

$$M_{\mathrm{a}}(\mathbf{q}) = \tfrac{1}{2}\left\langle \left(\mathbf{q}\cdot\mathbf{u}^{\mathrm{a}}\right)^2 \right\rangle. \quad (4)$$

The temperature dependences of the peak area of the X-ray line scans are shown in Fig. 1. This dependence is reproduced fairly well by the calculated $\langle u^2 \rangle$ for InN as shown with dashed lines in Fig. 1. Parameter B's in formula (2) were refined to fit the measured data as shown with solid lines in Fig. 1. The

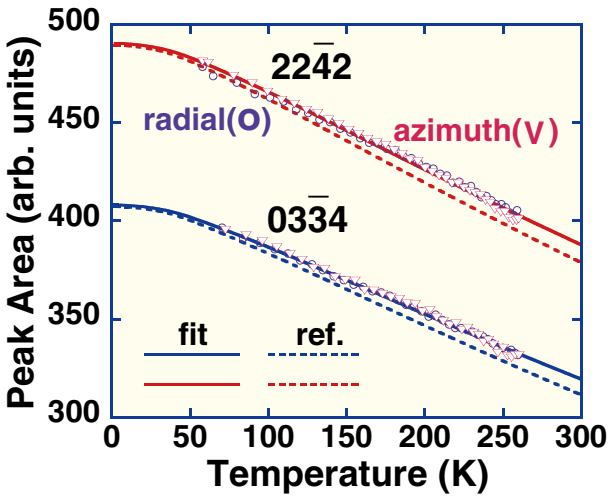

Fig. 1: Peak area of InN 222 and 034 reflections as a function of temperature. All of lines are calculated from $\langle u^2 \rangle$ in Fig. 2

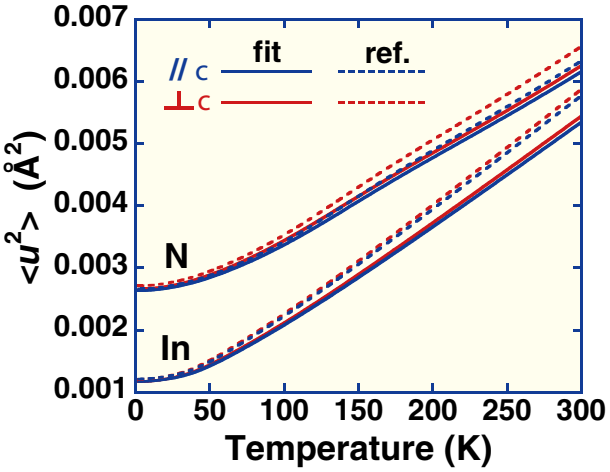

Fig. 2: $\langle u^2 \rangle$ of In and N atoms as a function of temperature obtained from this work (solid lines) and Ref. [3] (dashed line)

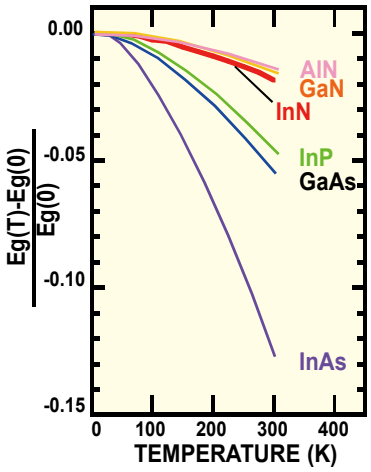

Fig. 4: Temperature dependence of band-gap energy in III-V semiconductors

theoretical calculations on $\langle u^2 \rangle$'s of InN (dashed lines in Fig. 2) and related materials (Fig. 3) show the $\langle u^2 \rangle$ of cation in InN are 0.4-0.8 times of that of InAs, InP, GaAs, and GaP [3,4]. For the anion, it is 0.6-1.0 times.

When the temperature is around or above Debye temperature, $\langle u^2 \rangle$ is inversely proportional to inter atomic force constant. The force constant of III-N is large owing to small anion N radius and bond length. Therefore, small $\langle u^2 \rangle$ of III-N is quite reasonable.

This suggests that the small dEg/dT of InN partly comes from small $\langle u^2 \rangle$ in comparison with that of InGaAsP.

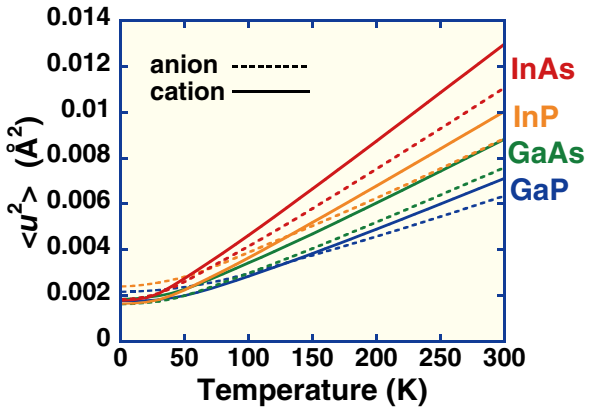

Fig. 3: Theoretically calculated $\langle u^2 \rangle$'s of InAs, InP, GaAs, and GaP as a function of temperature.

The temperature dependence of band-gap energy in III-V semiconductors is shown in Fig. 4. This dependence is normalized with the band-gap energy of each material at the absolute zero temperature. The dependence of InN, which is investigated from our measurements of optical absorption, is also shown. The above result can support Fig. 4. Therefore, nitride semiconductors including InN can be expected to be applied for temperature-stable devices. The optical characteristics of InN show the perspective in the realization of laser diodes for dense-wavelength-division multiplexing (D-WDM) system, temperature-stable solar-cells, and so on.

References

[1] J. Wu *et al.*, *J. Appl. Phys.* **94,** 4457 (2003).
[2] Y. Zhang *et al.*, *Phys. Stat. Sol.* (c) **8,** 482 (2011).
[3] M. Schowalter *et al.*, *Acta Cryst.* A**65,** 227 (2009).
[4] M. Schowalter *et al.*, *Acta Cryst.* A**65,** 5 (2009).

Keywords: nitride semiconductors, energy gap, X-ray diffraction, white LEDs, green LEDs, solar Cells, infrared LDs
Takashi Matsuoka (Physics of Electronic Materials Division)
E-mail: matsuoka@imr.tohoku.ac.jp
http://www.matsuoka-lab.imr.tohoku.ac.jp/

Giant Spin-Hall Effect in Impurity Doped-Au

Highly efficient generation, control and detection of spin current, which is the flow of spin angular momentum, are essential issues to develop spintronic devices with high performance and multi-functionality. Spin-Hall effect (SHE) enables us to convert between charge current and spin current in nonmagnetic materials without using a ferromagnetic material. The perpendicularly spin-polarized FePt/Au devices show giant SHE in Au. One of the possible origins for giant SHE is skew scattering by impurities in Au. Pt-doped Au shows significant thickness dependence of SHE, suggesting the importance of surface and/or interface scattering due to Pt atoms on the Au surface. In the case of Fe-doped Au, on the other hand, the impurity concentration dependence and thickness dependence of SHE imply that the resonant skew scattering in bulk mainly contributes to the large SHE.

"Spintronics", which utilizes the freedom of spins, provides electronic devices with novel functionality. In the research field of spintronics, the generation, control and detection of the flow of spin angular momentum (i.e. "spin current") are key issues to develop high performance devices. Recently, spin-Hall effect (SHE) in nonmagnetic materials has attracted much attention since SHE enables us to generate or detect pure spin current without using a ferromagnetic material.

SHE is generally considered to the same origin as that for the anomalous Hall effect (AHE). The most distinguished point of SHE is that it does not require ferromagnetic order. When charge current flows in a nonmagnetic material having large spin-orbit coupling, electrons are scattered in the transverse direction. The scattered directions are opposite between up- and down-spin electrons. Consequently, spin current appears in the transverse direction to the charge current, which is called the direct SHE (DSHE). On the other hand, spin current induces the transverse charge current, which is called the inverse SHE (ISHE). The electrical detection of SHE was reported in several nonmagnetic metals [1-6]. Previously, we reported the giant SHE in Au employing lateral devices with an FePt perpendicular spin injector and a Au Hall cross [4]. Theories [7,8] have suggested that the impurities in Au play a significant role for the enhancement of the spin-Hall angle (α_H).

In order to understand the mechanism of the giant SHE in Au, we have investigated SHE in Pt-doped and Fe-doped Au. The devices, consisting of an FePt perpendicular spin injector and a doped Au Hall cross, were prepared on an MgO (100) substrate. Thin films were prepared employing an ultrahigh vacuum magnetron sputtering system. Nanometer-sized devices were fabricated using electron beam lithography and Ar ion milling. The thickness of the Hall cross (t_N) was varied in the range from 10 nm to 30 nm. Fig. 1(a) shows a scanning microscope image for the device. The measurement setup is also shown in Fig.1(a). The electric current was applied from FePt to

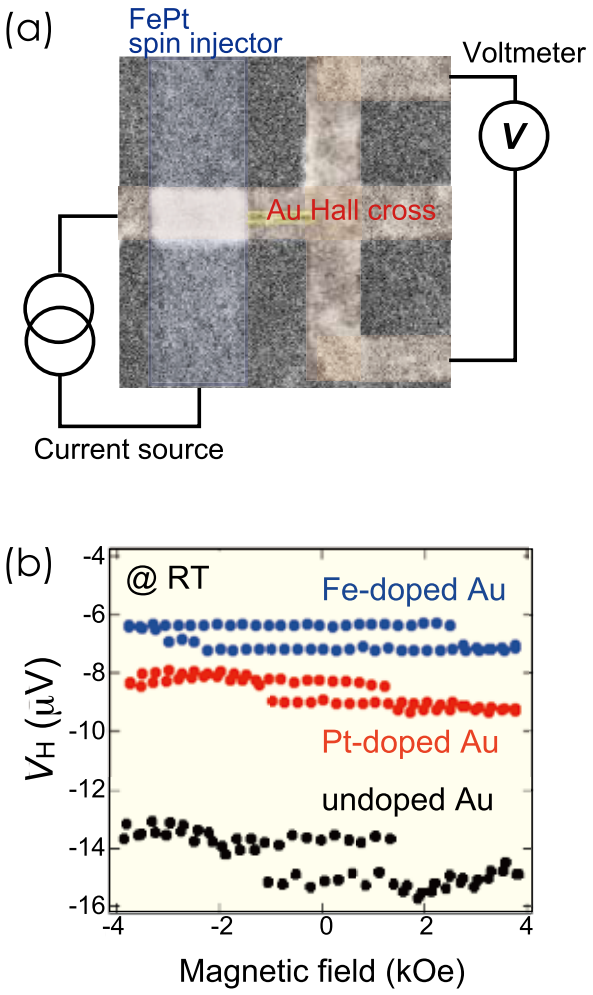

Fig. 1: (a) A scanning microscope image for the device with an FePt perpendicular spin injector and a doped Au Hall cross. The measurement circuit is also shown. (b) Non-local voltage (V_H) as a function of perpendicular magnetic field for the devices with 0.4 at.% Pt-doped, 0.4 at.% Fe-doped, and undoped Au.

Au. This induced spin accumulation around the interface between FePt and Au, resulting in the diffusion of spin current even in the Au Hall cross where charge current did not flow. This means that pure spin current is generated in the Au

Hall cross. The pure spin current was converted into charge current due to ISHE in Au, and non-local voltage appeared in Au.

Fig. 1(b) displays the non-local voltage (V_H) as a function of perpendicular magnetic field for the devices with 0.4 at.% Pt-doped, 0.4 at.% Fe-doped, and undoped Au. All the devices show the clear hysteresis of V_H, which reflects the magnetization reversal of the FePt perpendicular spin injector. These results indicate that ISHE converts the spin current into the charge current even for doped Au. From the analysis of V_H as a function of the distance between FePt and Au Hall cross, the values of α_H were estimated for undoped and doped Au. Undoped Au with t_N = 10 nm showed α_H = 0.07 ± 0.02. The value of α_H did not remarkably depend on the concentration of the Fe impurity [9], which is consistent with the theory predicting the resonant skew scattering [7]. On the other hand, α_H gradually increased with the concentration of the Pt impurity, and α_H = 0.14 ± 0.04 was obtained for 3 at. % Pt-doped Au, suggesting that the doping of Pt impurity leads to the enhancement of α_H.

Fig. 2 shows the thickness dependence of α_H for Pt-doped Au. In the case of Pt-doped Au, α_H decreased remarkably with increasing t_N. This implies that the contribution of the surface and/or interface scattering plays an important role for the enhancement of α_H. A theory predicts that the Pt atoms on the Au (111) surface provides the enhancement of spin-orbit coupling, which may explain the remarkable thickness dependence of SHE in Pt-doped Au [10]. In contrast to the results of Pt-doped Au, Fe-doped Au showed no dependence of α_H on t_N, implying that the resonant skew scattering in bulk mainly contributes to the large SHE in Fe-doped Au.

We found that the remarkable enhancement of α_H was observed for Pt-doped Au. Our finding is important to find a new route for further enhancement of SHE, which opens the way for the development of spintronic devices with high performance and multi-functionality.

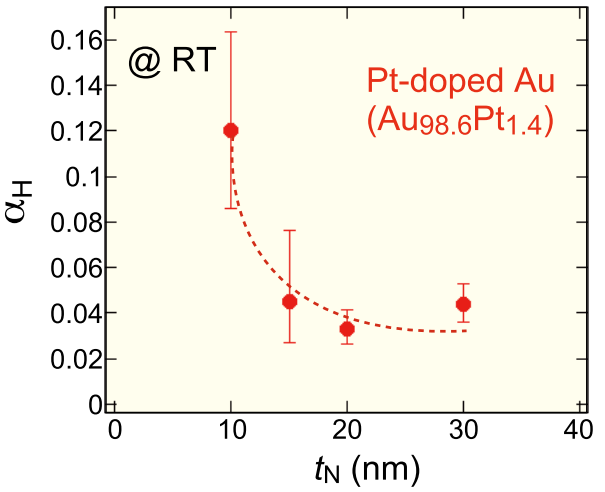

Fig. 2: The thickness (t_N) dependence of spin-Hall angle (α_H) for 1.4 at% Pt-doped Au. The measurement was carried out at room temperature.

References

[1] S. O. Valenzuela and M. Tinkham, Nature 442, 176 (2006).
[2] E. Saitoh, M. Ueda, H. Miyajima and G. Tatara, Appl. Phys. Lett., 88, 182509 (2006).
[3] T. Kimura, Y. Otani, T. Sato, S. Takahashi and S. Maekawa, Phys. Rev. Lett., 98, 156601 (2007).
[4] T. Seki, Y. Hasegawa, S. Mitani, S. Takahashi, H. Imamura, S. Maekawa, J. Nitta, and K. Takanashi, Nature Mater., 7, 125 (2008).
[5] M. Morota, K. Ohnishi, T. Kimura, and Y. Otani, J. Appl. Phys. 105, 07C712 (2009).
[6] Y. Niimi, M. Morota, D. H. Wei, C. Deranlot, M. Basletic, A. Hamzic, A. Fert, and Y. Otani, Phys. Rev. Lett., 106, 126601 (2011)
[7] G.Y. Guo, S. Maekawa, and N. Nagaosa, Phys. Rev. Lett., 102, 036401 (2009).
[8] M. Gradhand, D. V. Fedorov, P. Zahn, and I. Mertig, Phys. Rev. Lett., 104, 186403 (2010).
[9] I. Sugai, S. Mitani, and K. Takanashi, IEEE Trans. Magn., 46, 2559 (2010).
[10] B. Gu, I. Sugai, T. Ziman, G. Y. Guo, N. Nagaosa, T. Seki, K. Takanashi and S. Maekawa, Phys. Rev. Lett., 105, 216401 (2010).

Keywords: spin current, nanostructure
Koki Takanashi (Magnetic Materials)
E-mail: koki@imr.tohoku.ac.jp
URL: http://www.magmatex.imr.tohoku.ac.jp/

Fermi Surface Properties of Paramagnetic $NpCd_{11}$ with a Large Unit Cell.

We succeeded in growing a high-quality single crystal of $NpCd_{11}$ with the cubic $BaHg_{11}$-type structure by the Cd-self flux method. From the magnetic susceptibility and specific heat experiments, this compound is found to be a 5*f*-localized paramagnet with the singlet ground state in the crystalline electric field (CEF) scheme. Fermi surface properties were measured using the de Haas-van Alphen (dHvA) technique. Long-period oscillations were observed in the dHvA frequency range of 9.1×10^5 to 1.9×10^7 Oe, indicating small cross-sectional areas of Fermi surfaces, which is consistent with a small Brillouin zone based on a large unit cell. From the dHvA and magnetoresistance experiments, the Fermi surface of $NpCd_{11}$ is found to consist of many kinds of closed Fermi surfaces and a multiply-connected-like Fermi surface, although the result of energy band calculations based on the 5*f*-localized $Np^{3+}(5f^4)$ configuration reveals the existence of only closed Fermi surfaces. The corresponding cyclotron effective mass is small, ranging from 0.1 to 0.7 m_0, which is consistent with a small electronic specific heat coefficient $\gamma \approx 10$ mJ/K^2·mol, revealing no hybridization between the 5*f* electrons and conduction electrons.

UCd_{11} is one of the first discovered uranium-based heavy fermion compounds with an antiferromagnetic ordering at T_N=5 K [1]. A strongly enhanced value of the electronic specific-heat coefficient γ (840 mJ/K^2·mol) was obtained from the specific heat above 7 K. The hidden order transitions of UCd_{11} were observed by applying hydrostatic pressure and magnetic fields, using a high-quality single crystal [2].

The neptunium compound $NpCd_{11}$ also crystallizes in the $BaHg_{11}$-type structure, as shown in Fig. 1(a). The lattice parameter of 9.288 Å in $NpCd_{11}$ is almost the same as that in UCd_{11}. The specific heat data with a small electronic specific heat coefficient γ=10 mJ/K^2·mol indicates no evidence of magnetic anomalies. The single crystals of $NpCd_{11}$ were grown by the Cd-self flux method, following the Np-Cd alloy phase diagram. Many $NpCd_{11}$ single crystals with about 5×4×2 mm^3 were obtained as shown in Fig. 1(b). We carried out the measurements of electrical resistivity, transverse magnetoresistance, specific heat, magnetic susceptibility, magnetization and de Haas-van Alphen (dHvA) effect to clarify the electronic properties, using a high-quality single crystal of $NpCd_{11}$ [3].

Fig. 2(a) shows the angular dependence of the transverse magnetoresistance at 0.1 K under 70 and 140 kOe, where the field is rotated from <100> to <110>. The magnetoresistance becomes minimum around <111> and <110>. The corresponding field dependence of the magnetoresistance for three field directions is shown in Fig. 2(b).

Scince the 5*f* electrons in $NpCd_{11}$ are localized, with the Np^{3+} ($5f^4$) configuration, the valence electrons are $6d^17s^2$ of Np and $4d^{10}5s^2$ of Cd, revealing an uncompensated metal. The magnetoresistance increases as $H^{1.1}$, revealing the existence of an open orbit along [110] in the configuration of $J//[1\bar{1}0]$ and $H//[001]$ and also in the other wide field angle region.

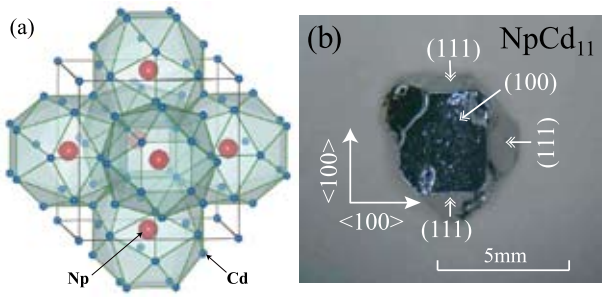

Fig.1. (a) Crystal structure of $NpCd_{11}$, where the Np atom is surrounded by 20 nearest and next-nearest neighbor Cd atoms, and (b) photograph of a $NpCd_{11}$ single crystal.

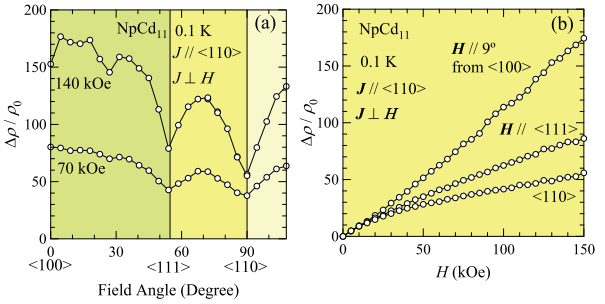

Fig.2. (a) Angular dependence of the transverse magnetoresistance at 0.1 K under the field of 70 and 140 kOe , and (b) field dependence of the transverse magnetoresistance at 0.1 K for *H*//<110>, <111> and <100>.

There exists, however, a question why the magnetoresistance does not indicate a clear H^2-dependence, even though the sample is of high quality. The Fermi surface properties are also discussed in the dHvA experiment.

In order to study furthermore the electronic state of $NpCd_{11}$, we performed the dHvA experiment at low temperatures. Seven fundamental dHvA branches are detected together with their harmonics. Among them, three dHvA branches are named α, γ and δ. By

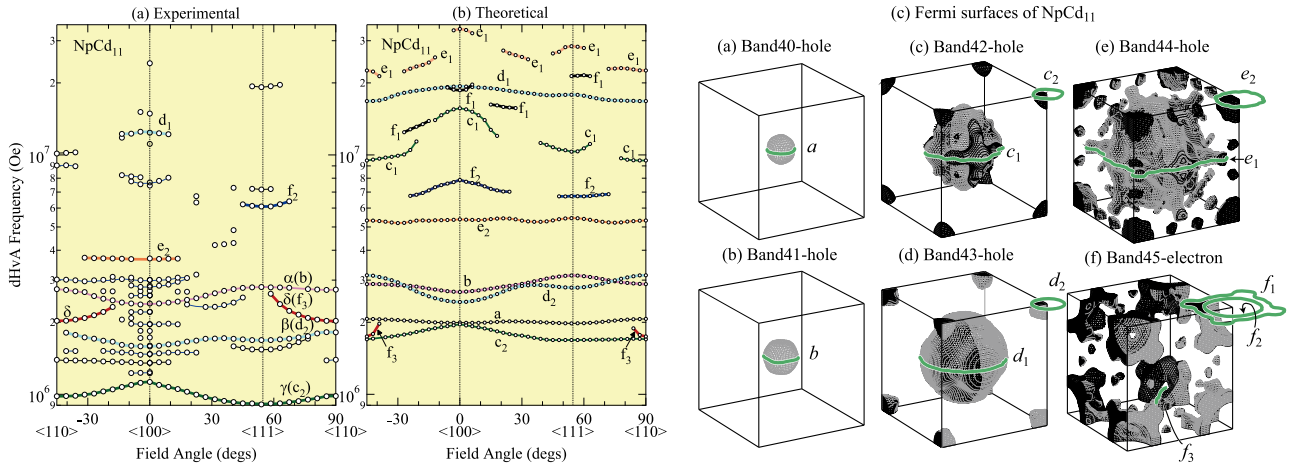

Fig. 3. Angular dependence of (a) the experimental and (b) theoretical dHvA frequencies in $NpCd_{11}$. (c) Theoretical Fermi surface of $NpCd_{11}$.

rotating the sample about the magnetic field, we determined the angular dependence of the dHvA frequencies in $NpCd_{11}$, as shown in Fig. 3(a). Here, we could not observe clear branch β for *H*//<110>, especially in the {100} plane. The dHvA frequencies are relatively small, ranging from 9.1×10^5 to 1.9×10^7 Oe.

Since $NpCd_{11}$ possesses small Brillouin zone due to a large lattice constant *a*=9.288 Å, the branches α, β and γ occupy small volumes, that is, approximately 0.97, 0.51 and 0.23%, respectively. This indicates that branches α, β and γ correspond to the small pocket Fermi surfaces. The dHvA frequency of branch δ has a minimum for *H*//<110>, and increases by tilting the field angle from <110>, indicating a cylindrical or ellipsoidal Fermi surface elongated along <110>. These branches are most likely due to the multiply-connected Fermi surfaces.

Here we note that the maximum dHvA frequency allowed in the present small Brillouin zone is $F_{max} = 3.8\times10^7$ Oe for the spherical Fermi surface. This means that the multiply-connected Fermi surfaces contribute to a large volume of the Fermi surface in the present small Brillouin zone of $NpCd_{11}$.

We determined the cyclotron effective mass from the temperature dependence of the dHvA amplitude for the principal field directions. The cyclotron effective masses are in the range from 0.11 to 0.68 m_0. These small values are consistent with the small γ value. The theoretical angular dependence of the dHvA frequency and the corresponding Fermi surface calculated from a fully-relativistic linear augmented-plane-wave (LAPW) method are shown in Fig. 3(b) and (c), respectively.

All the theoretical Fermi surfaces are thus closed Fermi surfaces, without multiply-connected Fermi surfaces. If these Fermi surfaces are correct, there exist no open orbits in the magnetoresistance. Here we remark a band 44-hole Fermi surface centered at the Γ point, possessing a slender arm along the <110> direction. One possibility is that this arm is elongated up to the Brillouin zone boundary and is multiply-connected along <110>. In this case, the open orbits are formed only in a small field-angle region around <110>.

References

[1] Z. Fisk et al., Phys. Rev. B **30** (1984) 6360.
[2] D. Aoki et al., J. Phys. Soc. Jpn. **68** (1999) 3117.
[3] Y. Homma et al., IOP Conf. Series: Mater. Sci. & Eng. **9** (2010) 012091.

Keywords: $NpCd_{11}$, transuranium compound, magnetoresistance, CEF, dHvA, fermi surface
Y. Homma (Radiochemistry of Metals)
E-mail: yhomma@imr.tohoku.ac.jp
URL:http:// http://www.imr.tohoku.ac.jp/ja/org/research/24.html

Direct Evidence of Elastic Interaction between Ferroelectric Domain and Misfit Dislocation

We have elucidated the elastic interaction between 90° domains and misfit dislocations in $PbTiO_3$/$SrTiO_3$ (001) epitaxial thin films by local strain mapping based on high-resolution transmission electron microscopy. A novel mechanism for the nucleation and growth of 90° domains has been proposed based on the results, including the introduction of an additional dislocation perpendicular to a misfit dislocation and the dissociation of these dislocations into two pairs of superlattice partial dislocations with an anti-phase boundary.

The nature of ferroelectric materials is attributable to the switching of domain configuration, in which spontaneous polarizations orientate in given directions. In domain rotation, actually domain walls move in a crystal, or new domains nucleate. It has been said that the motion or the nucleation of domain walls are pinned by some defects, such as misfit dislocations, owing to the elastic interaction between them. Then, it is important to quantify the elastic interaction between domains and defects in order to understand the dynamics and the nucleation and growth of the domains [1-4]. This paper illustrates the structure of a 90° domain just on a misfit dislocation at the atomic resolution, and elastic interactions between them using electron microscopy and related strain mapping techniques [5].

Atomic configuration around 90° domain and dislocations [6]

$PbTiO_3$ epitaxial thin films were deposited on $SrTiO_3$(001) single crystal substrates using pulsed metalorganic chemical vapor deposition (MOCVD) [7]. Fig. 1 shows aberration-corrected HRTEM (high resolution transmission electron microscope) and HAADF-STEM (high angle annular dark field-scanning transmission electron microscope) images around an *a*-domain, which means a 90° domain, near the interface with edge-type dislocations. The inset in (c) marks an anti-phase boundary (APB) along a $(\bar{1}01)$ plane, where atomic columns are shifted by a half of the lattice period. This *a*-domain is about 3 nm wide. The lattice plane in the *a*-domain is strongly deflected inside the 3 nm band because of the large tetragonality of $PbTiO_3$. HAADF-STEM image of Fig. 1(c) clearly shows that lattice rotation takes place across the 90° domain wall, and that it stems from the lattice rotation around the core of the dislocations. HRTEM images in Figs. 1(a) and (b) show weak contrasts at the $PbTiO_3$/$SrTiO_3$ interfaces. HAADF-STEM image of figure 1(c) clearly shows an atomic level relationship between the interface and the dislocations. In an early study, it was reported that, in this system, the misfit dislocation is often an edge-type perfect dislocation with Burgers vector

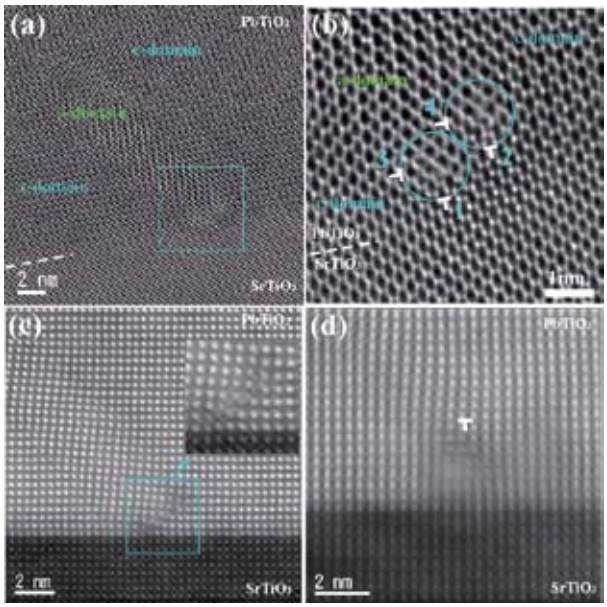

Fig. 1: (a) Aberration-corrected HRTEM image around the $PbTiO_3$/$SrTiO_3$ interface, (b) magnified image of the squared region in (a). (c) HAADF-STEM image around edge dislocations with an *a*-domain. The inset is a blow-up of the squared region in (c). (d) shows an edge-type dislocation without any *a*-domain. a- and c-domain have polarizations in the in-plane and out-of-plane directions, respectively.

b=**a**[100] [1]. Fig. 1(d) shows that a misfit dislocation without an *a*-domain is the perfect dislocation with Burgers vector **b**=**a**[100] corresponding to the edge of the unit cell. The extra double-plane is composed of a pair of Pb–O and Ti–O layers. However, the misfit dislocation with an *a*-domain in figures 1(a)–(c) is dissociated into a couple of edge-type partial dislocations at the bottom end of the *a*-domain (No. 1 and No. 2). Furthermore, additional edge-type partial dislocations No. 3 and No. 4 are introduced after the growth of *a*-domain. This result implies that edge-type dislocation with Burgers vector **b**=**a**[001] can be introduced and dissociated into a pair of edge-type partial dislocations. Extra half-planes of Pb–O or Ti–O layers are inserted at the substrate and the left, parallel to (100) and (001) planes, respectively. Considering the

contrast of the atomic columns in Fig. 1(c), extra half-planes of Ti–O are inserted in the partial dislocations No. 1 and No. 3, and those of Pb–O in the partial dislocations No. 2 and No. 4. The atomic arrangement on the ($\bar{1}$01) plane between these partial dislocations is shifted by a half of the $PbTiO_3$ unit cell. In our observations, all the *a*-domains immediately above the $PbTiO_3/SrTiO_3$ interface are accompanied with two pairs of superlattice partial dislocations with an APB parallel to the ($\bar{1}$01) plane.

Elastic Interaction of 90° domain with dislocations [6]

Fig. 2 shows a strain mapping by GPA of Fig. 1(a); namely, (a) the normal strain in the in-plane direction ε_{xx}, (b) that in the out-of plane direction ε_{yy}, (c) the share strain ε_{xy} and (d) the rigid rotation ω_{xy}. These strain values show deviation of the lattice parameter from the $SrTiO_3$ reference. The ε_{xx} map clearly shows the *a*-domain. The strain field ε_{xx} around the partial dislocation corresponds to that of the dislocation No. 1 and No. 2. The strain field ε_{xx} under tension around the partial dislocation is coupled with that of the *a*-domain. The ε_{yy} map shows that the lattice parameter along the *a*-axis in the a-domain is almost the same as in the $SrTiO_3$ substrate. The strain field ε_{yy} around the partial dislocation corresponds to that of the dislocations No. 3 and No. 4. The compressed side of the strain field ε_{yy} is coupled with the a-domain. The ε_{xy} map shows no strain around the a-domain, but around the misfit dislocation. There is no elastic interaction between the a-domain and the dislocations through share strain. The ω_{xy} map shows that the lattice of the *a*-domain rotates counterclockwise against the *c*-domain and the substrate. The lattice rotation around the dislocations is coupled with that of the *a*-domain. These strain maps elucidate that the 90° domain interacts with dislocations attractively.

These results indicate that the lattice rotation around the core of the misfit dislocation with the Burgers vector **b**=**a**[100] triggers the nucleation of the 90° domain, and the strain matching with the misfit dislocation assists domain growth. Then, an additional edge dislocation with Burgers vector **b**=**a**[001] is introduced to compensate the lattice rotation of 90° domain. After that, an APB is introduced by the dissociation of full dislocations into two pair of superlattice partial dislocations for the lattice matching at the bottom interface of a-domains.

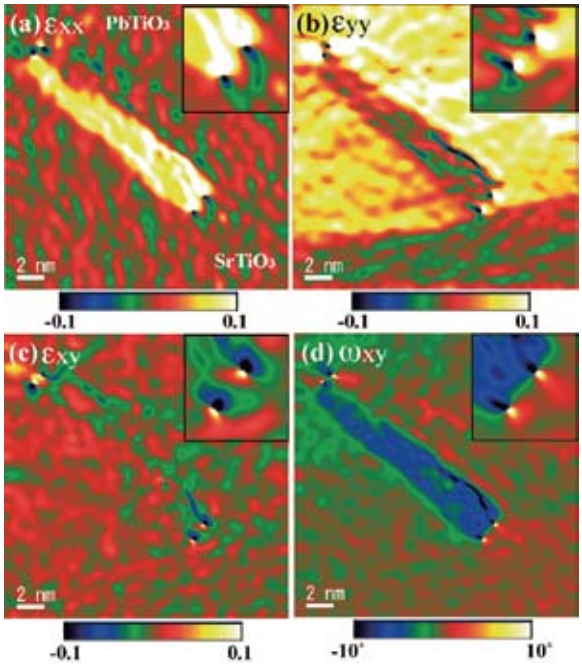

Fig. 2: Strain mapping of Fig. 1(a) around an a-domain near the film/substrate interface; namely (a) normal strain in the in-plane direction ε_{xx}, (b) that in the out-of plane direction ε_{yy}, (c) share strain ε_{xy} and (d) rigid rotation ω_{xy}. Insets in (a)-(d) are magnified strain fields around dislocations.

Thus, our atomic-scale analysis provides a direct evidence on the elastic interaction between an *a*-domain and a misfit dislocation, and on domain nucleation and growth mechanisms.

References

[1] S. Stemmer, S. K. Streiffer, F. Ernst and M. Rühle, phys. stat. sol. (a), **147**, 135 (1995)
[2] S. Stemmer, S. K. Streiffer, F. Ernst and M. Rühle, W. Y. Hsu and R. Raj, Solid State Ionics (a), **75**, 43 (1995)
[3] I. B. Misirlioglu, A. L. Vasiliev, S. P. Alpay, M. Aindow and R. Ramesh, J. Mater. Sci. **41**, 697 (2006)
[4] A. Yu. Emelyanov and N. A. Pertsev, Phys. Rev. B, **68**, 214103 (2003)
[5] M. J. Hÿtch, E. Snoeck and R. Kilaas, Ultramicroscopy, **74**, 131 (1998)
[6] T. Kiguchi, K. Aoyagi, Y. Ehara, H. Funakubo, T. Yamada, N. Usami, and T. J. Konno, Sci. Technol. Adv. Mater. **12**, 034413 (2011).
[7] H. Nakaki, YK. Kim, S. Yokoyama, R. Ikariyama, H. Funakubo, K. Nishida, and KSaito, Appl. Phys. Lett. **91**, 112904 (2007).

Keywords: ferroelectric, defects, transmission electron microscopy
T.Kiguchi (Advanced Analysis of Materials)
E-mail: tkiguchi@imr.tohoku.ac.jp
URL: http://konno-lab.imr.tohoku.ac.jp/

Electron-Hole Asymmetry of Spin Correlation in High Transition Temperature Superconductors

Spin correlations in both electron- and hole-doped Mott insulator have been studied by single crystal neutron scattering measurement. We succeeded in observing the spin fluctuation in the new target system of Bi2201. The qualitative analysis clarified the similarity of incommensurate correlation in Bi2201 and La214, suggesting a common doping-evolution of spin correlation in the single-layer hole-dope system. On the other hand, commensurate spin fluctuation was observed in a wide energy region of electron-dope PrLa214 system. Therefore, there exists intrinsic electron-hole asymmetry in the spin correlation against carrier doping.

High-transition-temperature (High-T_C) superconductivity in cuprate oxide emerges by doping sufficient charge carriers into an antiferromagnetic (AF) Mott insulator. Therefore, the doping evolution of spin correlation and its role in the mechanism of superconductivity have been intensively studied. Neutron-scattering measurement, which is powerful technique for the investigation of spin correlations, clarified an intimate relation between magnetism and superconductivity. An existence of spin excitation showing the similar hourglass-shaped spectrum in the different class of hole-doped superconductors $La_{2-x}Sr_xCuO_4$ (La214) [1] and $YBa_2Cu_3O_{6+\sigma}$ [2] indeed suggests the importance of spin fluctuations for the appearance of high-T_C superconductivity

To confirm the universal nature in the spin excitation spectrum and to understand the superconducting mechanism, further systematic measurements on other reference compounds are necessary. However, difficulties in growing sizable single crystal become bottleneck of the neutron-scattering study, since inelastic measurement requires large volume of sample over 1cc. We, therefore, attermpted to grow single crystal of several systems with the aim of investigation of entire spin excitation at newly constructed high-flux neutron facilities such as J-PARC.

Here, we introduce a recent progress in the study of spin correlations in new target systems of single-layer $Bi_{2+x}Sr_xCuO_{6+\sigma}$ (Bi2201) [3] and $Pr_{1-x-y}La_yCe_xCuO_4$ (PrLa214) [4], which is brought by the success of crystal-growth (Fig. 1(a)) and development of neutron-scattering techniques.

Universal spin correlation in insulating phase of hole-doped single-layer system

Dynamic spin correlation in the Bi2201 was studied to clarify the universal magnetism at lightly hole-doped region of cuprate oxide. We have succeeded in observing incommensurate (IC) spin fluctuation in the spin-glass sample of Bi2201 for the first time [5]. (Fig. 1(b)) The modulation vector was found to be diagonal to Cu-O bonding direction, similar to the observation in La214. Incommensurability corresponding to the peak-splitting is also consistent with the value for La124 with the comparable hole concentration. Therefore, we concluded that IC spin correlation commonly develops in the spin-glass phase of single layer cuprate by hole-doping. The geometry of observed IC peaks in the (h,k,0) reciprocal plane is quite similar to that in insulating single layer compound $La_{2-x}Sr_xNiO_4$ (Fig. 2), suggesting that strong-coupling physics is more relevant to the origin of IC magnetic peak in the spin-glass phase of cuprate oxide.

Characteristic high-energy spin fluctuations in

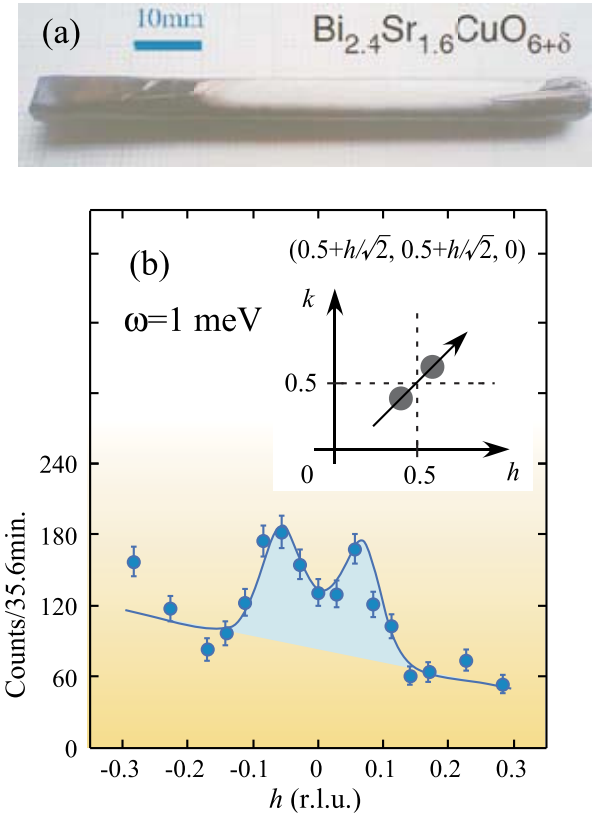

Fig. 1: (a) Single crystal of $Bi_{2.4}Sr_{1.6}CuO_{6+\delta}$ and (b) the neutron scattering spectrum measured at ω=1 meV and 6 K.

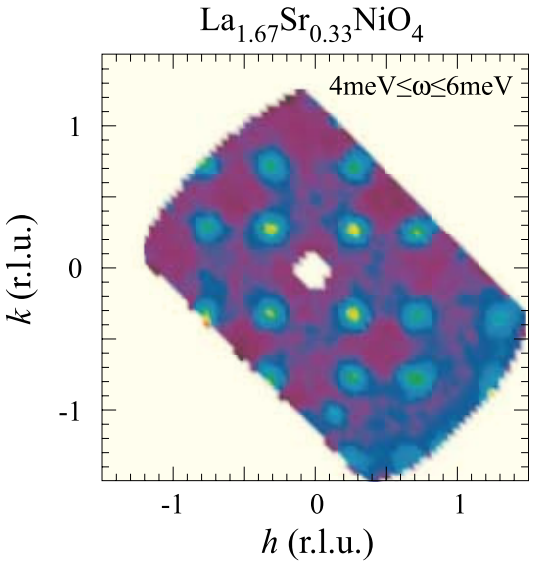

Fig.2: Neutron scattering intensity from $La_{1.67}Sr_{0.33}NiO_4$. The spectrum sliced with the energy transfer between 4meV and 6meV is shown in (h, k) reciprocal plane.

electron-doped cuprate oxide

Up to now, many key measurements by neutron scattering have been lacking for the electron-doped system, due to the experimental difficulties. Therefore, the universal magnetic properties of high-*Tc* cuprate irrespective of the type of carriers are still controversial. To make a progress in the study of spin correlation, we have carried out a comprehensive neutron scattering measurement on the PrLa214 system [6].

Fig. 3 shows a neutron scattering intensity measured for the electron-doped AF ordered phase of PrLa214. We clarified the existence of high-energy spin fluctuations at least up to 150meV. Throughout the entire energy range, a single peak centered at the (0.5,0.5) position in the tetragonal unit was observed (Figs. 3(b) and (c)), unlike to the hourglass-shaped excitation in the hole-doped system. Therefore, the doping dependence of spin fluctuations at high-energy region in the two systems is different and such a distinct doping evolution suggests the existence of electron-hole asymmetry in the spin correlation in the wide energy scale. The characteristics of the magnetism and its relation to the superconductivity would be different in nature in the two systems.

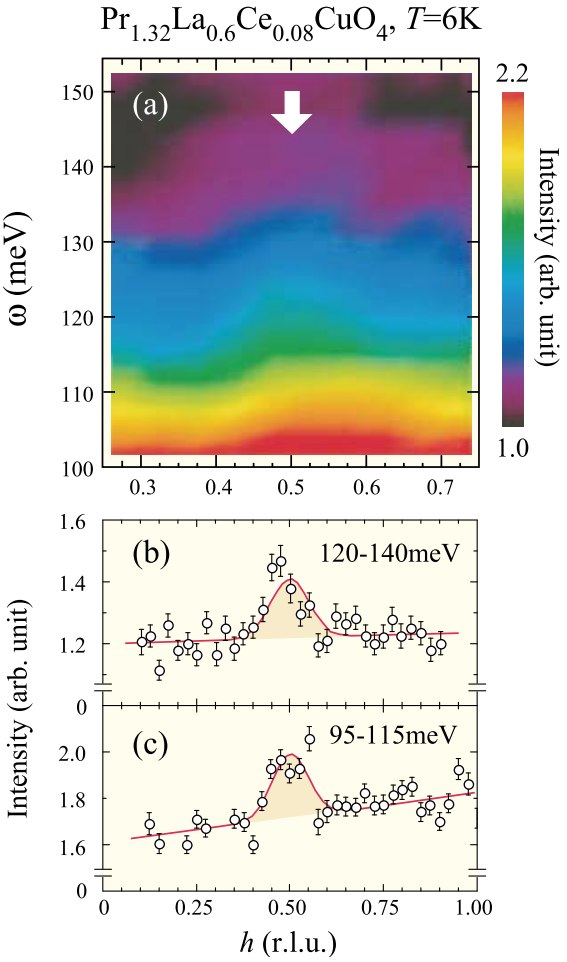

Fig.3: (a) Inelastic neutron scattering spectra of electron-doped AF ordered $Pr_{1.32}La_{0.6}Ce_{0.08}CuO_4$ in the energy and momentum space. Horizontal axis is parallel to [110] direction. Constant energy spectra sliced with (b) 130±10meV and (c) 105±10meV.

References

[1] J.M. Tranquada et al., Nature **375** (2004) 531.
[2] S.M. Hayden et al., Nature **375** (2004) 534.
[3] M. Enoki., et al., Physica C **470** (2010) S37.
[4] M. Fujita., et al., Phys. Rev. B **67** (2003) 014514.
[5] M. Enoki., et al., to appeare in JPSJ (Supplement).
[6] M. Fujita., et al., Phys. Rev. Lett. **101** (2008) 107003, M. Fujita., et al., to appeare in JPSJ (Supplement).

Keywords: neutron scattering, high-tc iron-based pnictide superconductors, spin excitation, crystal growth,
M. Fujita (Materials Materials Processing and Characterization)
E-mail:fujita@imr.tohoku.ac.jp
URL:http://www.imr.tohoku.ac.jp/ja/org/research/27.html,http://www.yamada-lab.imr.tohoku.ac.jp/jp/index.html

Effect of Current on Coulomb Oscillation in a Ni-Nb-Zr-H Glassy Alloy with Multiple Junctions.

The effect of current on Coulomb oscillation in a $(Ni_{0.36}Nb_{0.24}Zr_{0.40})_{90}H_{10}$ glassy alloy was carried out under currents of 1 nA, 10 nA, 100 nA, 1μA, 10μA, 100μA, 1mA, 10 mA and 100 mA in the temperature range of 300 to 6 K. The amplitude of the Coulomb oscillation showed maximum values at around 1μA. The discrete variation of the oscillation can be described as $E=2x10^{-4}exp(2.34N)$ ($r^2=0.993$), showing clear quantization of Coulomb oscillation, where E and N are the unit of $h/2e^2$ and step number, respectively. We suggested that quantization of conductance would be associated with nanometer-sized RC circuits in the alloy [1].

The quantum blockade effect by quantum-dot tunneling is one of the topics currently attracting a great deal of interest in the field of physics. Recently, Fukuhara *et al.* have observed the electric current-induced voltage oscillation in $((Ni_{0.6}Nb_{0.4})_{0.7}Zr_{0.3})_{1-y}H_y$ glassy alloys (with $0.052 \leq y \leq 0.152$) at temperatures below 240 K[2] and at room temperature[3]. From atomic bonding data in XAFS(X-ray Absorption Fine Structure)[4] using strong radiation photons of Spring 8, and a Nyquist diagram (Cole-Cole plot) by ac impedance analysis using a LCR meter [5], we proposed that quantum dot tunneling is charging and discharging the vacancy capacitance of Zr(Nb)-H-□-H- Zr(Nb) atomic bond arrays among the electric-conducting distorted icosahedral $Zr_5Ni_5Nb_3$ clusters (dots of ~0.55 nm in size [4]), where □ is the vacancy tunnel with regular prism of 0.23 nm, in the glassy alloys. Thus, we regarded it as a DC/AC converting device with a large number of nsnometer size capacitors.

To investigate the effect of Current on Coulomb Oscillation in eccentric glassy alloys, we determined the specific electrical resistance of $(Ni_{0.36}Nb_{0.24}Zr_{0.40})_{90}H_{10}$ glassy alloy consisting of nanometer-sized clusters by the four-probe method with a dc current of ±1 nA, ±10 nA, ±100 nA, ±1 μA, ±10 μA, ±100 μA, ±1 mA, ±10 mA and ±100 mA at cooling and heating rates of 1 K/s from 373 K to 6 K [1].

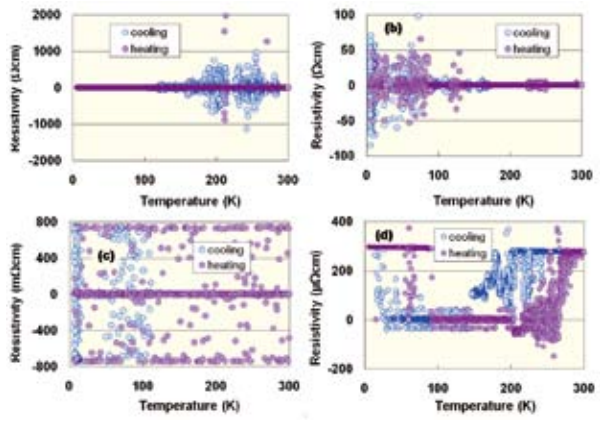

Fig.1 Electrical resistivities of $(Ni_{0.36}Nb_{0.24}Zr_{0.40})_{90}H_{10}$ glassy alloys under (a) ±1 nA, (b) ±1 μA, (c) ±1 mA and (d) ±100 mA dc current.

The representative current-dependent resistivities are shown as a function of temperature (Fig.1). These curves are composed of two kinds of curves, linear and abnormal oscillation ones. The linear curves follow Ohmic law whereas the abnormal curves do not. The abnormal curves represent dc current-induced Coulomb oscillation, which is associated with the quantum mechanism of solute hydrogen, although the restricted temperature region is different.

The temperature coefficients of resistivity (TCR) for linear curves with a semiconducting character in Fig. 1 are presented in Fig. 2(a). The decrement in TCR suggests an enhancement of the Debye-Waller factor, which is a characteristic of amorphous solids. The reason for the enhancement may be due to the pseudo-localization effect of an electron in an extremely small electric current such as 1 nA. It is known that an electron-electron interaction by localization effect causes an increase in electrical resistivity accompanied by elastic scattering.

The maximum amplitude (voltage) of the Coulomb oscillation (Fig. 2(b)) in Fig. 1 increases as the current decreases down to 1mA and then shows a plateau between 1 mA and 1 μA, and finally decreases in the lower current region from 100 to 1 nA, indicating an occurrence of the optimum current for quantum dot tunneling between the icosahedral $Zr_5Ni_5Nb_3$ cluster islands.

As can be seen from Fig. 1, the oscillation showed discrete variation. The pronounced resistances quantized in the unit of $h/2e^2$ (R) for currents of 1 and 10 nA in Fig.1 are plotted in Fig. 3, as a function of step number (N). The

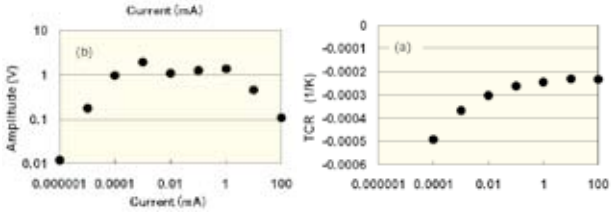

Fig.2 Effects of current on TCR (a) and maximum resistivity (b).

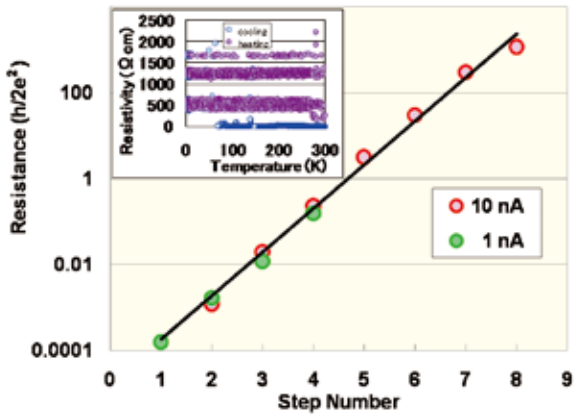

Fig.3 Relation between quantized resistance (R) and step number (N) for the $(Ni_{0.36}Nb_{0.24}Zr_{0.40})_{90}H_{10}$ glassy alloys under ±1 and 10 nA. Insert: Temperature dependent resistivity for 10 nA.

Coulomb oscillation for 10 nA is shown in the insert in Fig. 3. The discrete voltage jumps by one order for each step. Both relations for 1 and 10 nA can be described as R=0.0002exp (2.34N) (r^2= 0.993), showing clear fractional quantization of resistance in Coulomb oscillation. We infer that the width of a narrow channel connecting three-dimensional reservoirs of electrons among the distorted icosahedral $Zr_5Ni_5Nb_3$ clusters increases when the current decreases, provided that the glassy alloy is composed of a high number of a nanometer- sized RC circuits constructed by a pair of pointed $Zr_5Ni_5Nb_3$ channels and perpendicularly connecting cluster array reservoirs which contain subnanometer-sized capacitors (Fig. 4).

To inspect quantum transport in glassy alloys of interest, we lastly analyzed the dynamic evolution of an ensemble of electrons performing macroscopic resonant tunneling for room-temperature millimeter-sized Coulomb oscillation in Ni-Nb-Zr-H glassy alloys as a function of the cluster size and boundary length, using a one-dimensional (1D) Kronig-Penny model with a stepwise potential [6]. Fig. 5 (a) shows the barrier number dependence of *Tn*. *Tn* shows nonstationary counter-rotating sinusoidal chaotic behavior in periodic units below and over a boundary number of around 3000. The reflection component of *S* matrix, $S_{11}(n)$, shows a quasi-periodic torus portrait in the complex plane of Fig.5 (b). Since the torus is an attractor of three-dimensional phase space, it manifests as macroscopic resonant tunneling of an ensemble of electrons through

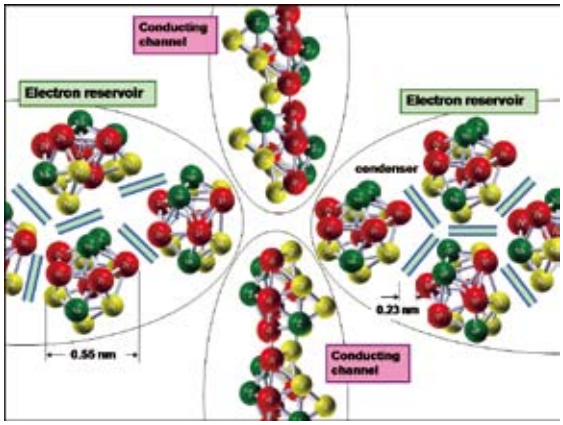

Fig.4 Configuration pattern of a nanometer-sized RC circuit constructed by a pair of pointed, negatively charged, distorted-icosahedral Zr5Ni5Nb3 cluster channels connecting both perpendicular cluster array reservoirs which are surrounded by capacitors shifting electron potential. Note: the Voronoi-type polyhedral portion is not shown.

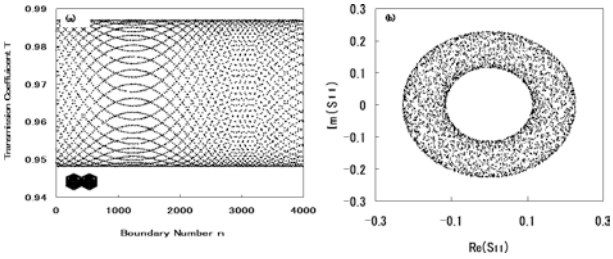

Fig.5 Transport properties of δ-function model for a=0.79, d=0.23 and F=3.52x10^{-6}. *Tn*; Insert: cluster array with a size of 0.55 nm and boundary distance of 0.23 nm; (b) $S_{11}(n) = \rho_n \exp(i\theta_n)$;

multi-barriers. Strictly speaking, the component wanders in a chaotic way in the torus space. Thus we believe that these results successfully explain the macroscopic resonant tunneling in Ni-Nb-Zr-H glassy alloys

References

[1] M.Fukuhara, and A.Inoue, Appl.Phys.Lett., **97**, 243108 (2010).
[2] M.Fukuhara, A.Kawashima,S.Yamaura and A.Inoue, Appl.Phys.Lett., **90**, 20311 (2007)
[3] M.Fukuhara and A.Inoue, J.Appl.Pjys., **105**, 063715 (2009).
[4] M.Fukuhara, N.Fujima, H.Oji, A.Inoue and S.Emura, J. Alloy Comp., **497**, 182 (2010).
[5] M.Fukuhara, M.Seto and A.Inoue, Appl.Phys.Lett., **96**, 043103 (2010).
[6] M.Fukuhara and M.Ban, Chaos, **20**, 033107 (2010).

Keywords: amorphous, electronic material, nanocluster
M.Fukuhara(Adv. Mater. Devel.& Integ. of Novel Struct. Met. and Inorg. Mat)
E-mail: Fukuhara@imr.tohoku.ac.jp
URL: http://www.xraylab.imr.tohoku.ac.jp

Conversion of Conduction Carriers from Holes to Electrons in $YBa_2Cu_3O_y$ Films Using an Electrochemical Technique.

A strong reduction of holes and an accumulation of electrons in $YBa_2Cu_3O_y$ films were made possible at room temperature by using an electrochemical doping technique. Using this technique, we succeeded in observing the superconductor-to-insulator transition in the hole-doped region, and in converting the sign of the conduction carriers from holes to electrons. Eventually we obtained a 'metallic' electron-doped YBCO film with the carrier density of 2.5 × 10^{20} cm^{-3} and the resistivity below 40 mΩcm.

High transition temperature (high-T_c) superconductivity in cooper oxides appears when the parent Mott insulators are doped with holes (*p*-type carriers) or electrons (*n*-type carriers). However, *p*-type and *n*-type cooper oxides in most cases differ not only in their doping dependence of magnetic and superconducting transitions but also in crystallographic structure [1-3]. For precise comparison with the theories for the origin of high-T_c superconductivity, a wide-range control of the carrier density, which contains the sign change of carriers, in an identical parent material is highly desired. Here, we demonstrate the first realization of an *n*-type metallic state in an $YBa_2Cu_3O_y$ (YBCO) film, which is known to be typical *p*-type superconductor with a maximum T_c ~ 90 K [4].

The standard methods for carrier control in the high-T_c copper oxides are chemical substitution and variation of oxygen content with heat treatment [5,6]. For further expansion of the doping region, we employed an electrochemical technique [4], as is shown in Fig. 1. In this technique, the sample and counter electrode (typically Pt) are immersed in an electrolyte and the strong electric field between the sample and the ions moved at the surface region by the voltage V_{EC} plays an important role. When V_{EC} is smaller than a threshold value, the ions at the sample surface form an electric double layer (EDL), which functions as an effective capacitor [7]. Recently, electric-field-induced superconductivity with the EDL structure has been reported [8,9]. On the other hand, when V_{EC} is higher, as is the case in this study, a conventional electrochemical reaction occurs. The advantage of this reaction is that it can be performed at a low temperature, and offer different reaction routes from the usual heat treatment for controlling materials.

The samples used in this work were *c*-axis oriented YBCO films with a thickness of 50 nm grown by rf magnetron sputtering on the (100) surfaces of $SrTiO_3$. As the starting materials, we prepared films with various *y* (oxygen contents; doping levels) [4]. In the electrolyte of $KClO_4$/PEO or Cs/PEO (where PEO = polyethylene oxide), we repeated the sequence of (i) applying the voltage V_{EC} between the YBCO film and the Pt electrode for a time t_{EC} at 300 K, (ii) measuring the temperature dependence of the resistivity $\rho(T)$, and (iii) measuring the Hall coefficient R_H at 100 K.

Fig. 2 shows the typical evolution of $\rho(T)$ with the total reaction time $t_{total} = \Sigma t_{EC}$ when *y* of the initial sample was ~6.45 (T_c = 54K) and V_{EC} =1.0 V was applied in $KClO_4$/PEO electrolyte.

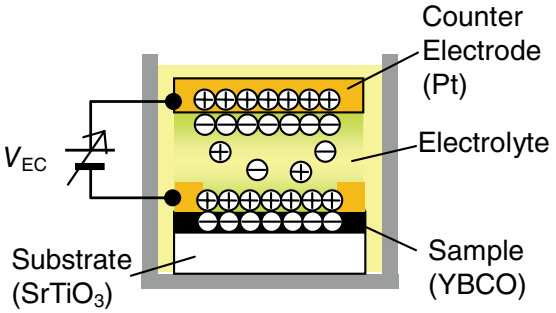

Fig. 1: Schematic drawing for the concept of the electrochemical reaction.

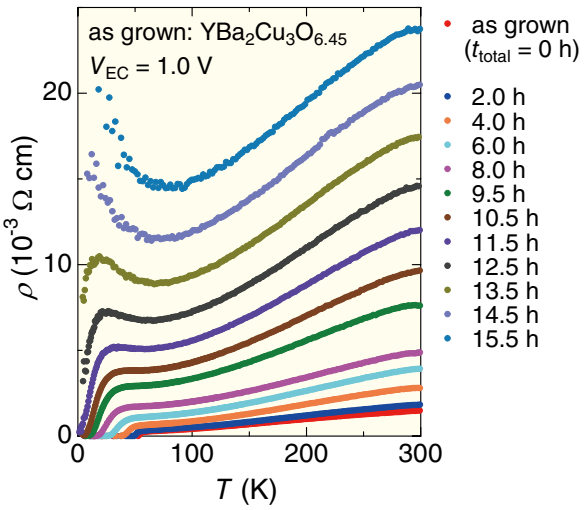

Fig. 2: Variation of the temperature dependence of resistivity $\rho(T)$ with total reaction time t_{total} in $KClO_4$/PEO electrolyte for the sample with the as-grown composition of $YBa_2Cu_3O_{6.45}$ (T_c = 54 K).

The remarkable features are the increase in ρ in the normal state by more than one order of magnitude and the decrease in T_c followed by the superconductor-to-insulator transition. Generally, such behaviour is associated with the reduction in the hole concentration. Indeed, a decrease in $1/eR_H$(100K), giving a relative measure for the carrier concentration, with t_{total} was observed.

Using this strong reduction process, we tried to realize *n*-type YBCO. Fig. 3 shows the variation of $\rho(T)$ as a function of t_{total} when *y* of the initial sample was ~6.2 (heavily underdoped) and V_{EC} =1.0 V was applied in $CsClO_4$/PEO. The as-grown sample exhibits a semiconductive behaviour of $\rho(T)$ with positive R_H. With increasing t_{total} up to 4 h, ρ increased significantly and became beyond the extent of our measurement. With a further increase of t_{total}, we observed a remarkable recovery of the electric conduction. It was also checked that $1/eR_H$(100K) decreases with t_{total} and crosses zero-doped point to a negative value at t_{total} > 4 h. These results strongly indicate that the carrier type changed from *p*-type to *n*-type around t_{total} = 4 h. ρ continued to decrease by more than four orders of magnitude, and eventually at t_{total} = 250 h, we obtained an *n*-type metallic YBCO film with $1/eR_H$(100K) = 2.5×10^{20} cm^{-3}.

Based on the data of X-ray diffraction and SIMS measurements [4], we conclude that the reduction of the oxygen content is the most plausible mechanism of the electrochemical doping, and that especially in the *n*-type region, YBCO films with $y < 6$, which cannot be attained in the usual heat treatment, is prepared. The present results provide firm evidence that the electrochemical method can pave a way toward ambipolar High-T_c copper oxide superconductors, which have never been synthesized yet.

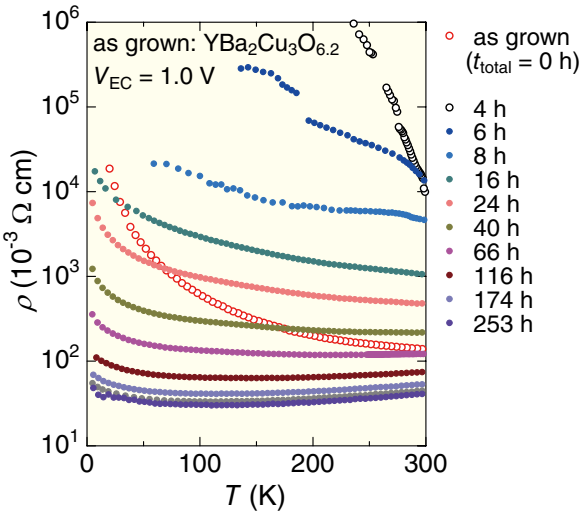

Fig. 3: Variation of the temperature dependence of resistivity $\rho(T)$ with total reaction time t_{total} in $CsClO_4$/PEO electrolyte for the sample with the as-grown composition of $YBa_2Cu_3O_{6.2}$.

References

[1] Y. Tokura, H. Takagi and S. Uchida, Nature **337**, 345 (1989).

[2] Y. Tokura, A. Fujimori, H. Matsubara, H. Watabe, H. Takagi, S. Uchida, M. Sakai, H. Ikeda, S. Okuda, and S. Tanaka, Phys. Rev. B **39**, 9704 (1989).

[3] H. Takagi, S. Uchida, and Y. Tokura, Phys. Rev. Lett. **62**, 1197 (1989).

[4] T. Nojima, H. Tada, S. Nakamura, N. Kobayashi, H. Shimotani, and Y. Iwasa, Phys. Rev. B **84**, 020502(R) (2011).

[5] K. Segawa and Y. Ando, Phys. Rev. B **74**, 100508 (2006).

[6] K. Segawa, M. Kofu, S.-H. Lee, I. Tsukada, H. Hiraka, M. Fujita, S. Chang, K. Yamada, and Y. Ando, Nature Phys. **6**, 579 (2010).

[7] H. Shimotani, H. Asanuma, A. Tsukazaki, A. Ohtomo, M. Kawasaki, and Y. Iwasa, Appl. Phys. Lett. **91**, 082106 (2007)

[8] K. Ueno, S. Nakamura, H. Shimotani, A. Ohtomo, N. Kimura, T. Nojima, H. Aoki, Y. Iwasa, and M. Kawasaki, Nature Mater. **7**, 855 (2008).

[9] J. T. Ye, S. Inoue, K. Kobayashi, Y. Kasahara, H. T. Yuan, H. Shimotani, and Y. Iwasa, Nature Mater. **9**, 125 (2010).

Keywords: electrical resistivity, doping, superconducting
T. Nojima (Laboratory of Low Temperature Materials Science)
E-mail: nojima@imr.tohoku.ac.jp